PRELIMINARY THREE-DIMENSIONAL DISCRETE FRACTURE MODEL OF THE TOPOPAH SPRING TUFF IN THE EXPLORATORY STUDIES FACILITY, YUCCA MOUNTAIN AREA, NYE COUNTY, NEVADA

by Lawrence O. Anna

U.S. GEOLOGICAL SURVEY

Open-File Report 97–834

Prepared in cooperation with the
NEVADA OPERATIONS OFFICE,
U.S. DEPARTMENT OF ENERGY, under
Interagency Agreement DE–AI08–92NV10874

Denver, Colorado
1998

U.S. DEPARTMENT OF THE INTERIOR
BRUCE BABBITT, Secretary

U.S. GEOLOGICAL SURVEY
Thomas J. Casadevall, Acting Director

For additional information write to:

Chief, Earth Science Investigations Program
Yucca Mountain Project Branch
U.S. Geological Survey
Box 25046, Mail Stop 421
Denver Federal Center
Denver, CO 80225-0046

Copies of this report can be purchased from:

U.S. Geological Survey
Information Services
Box 25286
Federal Center
Denver, CO 80225

CONTENTS

FIGURES

TABLES

CONVERSION FACTORS AND VERTICAL DATUM

Multiply	By	To obtain
centimeter (cm)	0.3937	inch
meter (m)	3.281	foot
kilometer (km)	0.6214	mile
square meter (m^2)	10.76	square foot
cubic meter (m^3)	35.31	cubic foot
meter squared (m^2)	9.87×10^{-13}	darcy
meter per second (m/s)	3.281	foot per second
meter squared per second (m^2/s)	10.76	foot squared per day
cubic meter per second (m^3/s)	35.31	cubic foot per second
meter per square meter (m/m^2)	0.3048	foot per square foot
square meter per cubic meter (m^2/m^3)	0.3048	square foot per cubic foot

Sea level: In this report "sea level" refers to the National Geodetic Vertical Datum of 1929 (NGVD of 1929)—a geodetic datum derived from a general adjustment of the first-order level nets of the United States and Canada, formerly called Sea Level Datum of 1929.

Preliminary Three-Dimensional Discrete Fracture Model of the Topopah Spring Tuff in the Exploratory Studies Facility, Yucca Mountain Area, Nye County, Nevada

By Lawrence O. Anna

ABSTRACT

Discrete-fracture modeling is part of site characterization for evaluating Yucca Mountain, Nye County, Nevada, as a potential high-level radioactive-waste repository site. Because most of the water and gas flow may be in fractures in low-porosity units, conventional equivalent-continuum models do not adequately represent the flow system. Discrete-fracture modeling offers an alternative to the equivalent-continuum method. This report describes how discrete-fracture networks can be constructed and used to answer concerns about the flow system at Yucca Mountain, including quantifying fracture connectivity, deriving directional-permeability distributions for one-and two-phase flow, determining parameters of anisotropy at different scales, and determining at what scale the rock functions as an equivalent continuum.

A three-dimensional discrete-fracture model was developed to investigate the effects of fractures on flow of water and gas in the Topopah Spring Tuff of Miocene age in the Exploratory Studies Facility at Yucca Mountain. Fracture data, used as model input, were taken exclusively from detailed line surveys in the Exploratory Studies Facility and converted into input parameters for simulation. A simulated fracture network was calibrated to field data. The simulated discrete fracture network was modified by eliminating nonconductive fractures determined from field-derived permeabilities. Small fractures also were removed from the simulated network without affecting the overall connectivity. Fractures, as much as 1.50 meters in length, were eliminated (a large percentage of the total number of fractures) from the network without altering the number of connected pathways. The analysis indicates that the fracture system in the Exploratory Studies Facility has numerous connected fractures that have relatively large permeabilities, but there are relatively few connected pathways across the simulated region. The fracture network was, therefore, sparse.

Directional permeabilites were calculated for flow regions that had scales ranging from 50 to 200 meters. Results of these calculations indicated that, for all scales, the east-west direction was the least conductive, whereas the top-bottom and the north-south directions were the most conductive. For the 200-meter scale, however, the north-south direction was the least conductive and the top-bottom direction was the most conductive. For the fracture network, none of the scales tested approached equivalent-continuum properties that are based on established criteria.

Two-phase flow simulations indicate that for different saturation extremes and for variable head boundaries, flux values from the low-saturation field were about 1.0 to 1.5 orders of magnitude lower from all traceplane face directions than flux values from the high-saturation field. With no-flow boundaries on the sides, flux values varied by two orders of magnitude when comparing flux calculated from low saturations to flux calculated from high saturations. Therefore, when specified head conditions were used at the

side boundaries, about one-half of flux was leaving the 200-meter block through the sides compared to flux through the bottom.

INTRODUCTION

Discrete-fracture modeling is part of the site characterization for evaluating Yucca Mountain, Nye County, Nevada as a potential high-level radioactive-waste repository site (fig. 1).

Flow models are also important for site characterization, repository design, construction, and performance assessment. Because most of the water and air flow is thought to be in fractures, instead of through the rock matrix, conventional equivalent continuum models may not adequately represent the true flow system at the potential repository site. Discrete-fracture models offer an alternative to the equivalent-continuum method, providing an accurate fracture geometry can be simulated. This report describes how discrete fracture networks (DFN) can be constructed and used to answer concerns, including quantifying fracture connectivity, deriving directional permeability distributions for one- and two-phase flow, determining parameters of anisotropy at different scales, and determining at what scale the rock functions as an equivalent continuum.

Construction of a DFN model requires synthesis of fracture data and well-test information from a variety of sources. This study used fracture mapping data to construct a computer-generated fracture network and simulate the flow through the fracture network for the Topopah Spring Tuff of Miocen age in the Exploratory Studies Facility (ESF) (fig 1). Fracture mapping in the ESF was the only data source that was used for input into the model. Borehole fracture mapping was not used. Hydraulic data were from air-permeability testing in two vertical boreholes near the ESF.

This study used the FRACMAN code, version 2.511 (Dershowitz and others, 1994), to produce stochastically generated three-dimensional discrete fracture networks (DFN's) at different scales. Stochastic modeling techniques have many possible outcomes, all or some of which can represent real conditions for a given set of geologically reasonable input parameters. Alternate outcomes delimit the range of uncertainty and can assess degrees of heterogeneity.

Flow modeling through the DFN was done using the flow code MAFIC, version 1.5 (Miller and others, 1994). The flow code MAFIC was coupled to the fracture-network model to simulate saturated flow conditions, to analyze the geometric configuration of the network, and to determine directional permeabilities and equivalent-continuum properties at various scales. For this study, connectivity analysis and flow solutions were made only on the conductive or connected network. Nonintersecting fractures were eliminated automatically in the finite-element meshing process using EDMESH (a module in FRACMAN) (Dershowitz and others, 1994).

Most of the problems of discrete-fracture modeling depend on computational efficiency and on meaningful parameter input. Identification, analysis, and simulation of thousands of fractures is extremely difficult. As a result, this study attempted to focus on the connectivity or conductivity of the network and not on the contribution of each fracture. That is, the study attempted to identify fractures that are part of the flow system as a function of the total volume and to eliminate fractures that are not part of the connectivity. Eliminating the small, nonconnecting fractures is more efficient and provides better matches with field data because most data-collecting techniques censor small fractures (except in borehole mapping).
This investigation was conducted by the U.S. Geological Survey in cooperation with the U.S. Department of Energy, under Interagency Agreement DE–AI08–92NV10874 as part of the Yucca Mountain Site Characterization Project.

Purpose and Scope

The purpose of this report was to: (1) Define the framework/geometry of the Topopah Spring Tuff flow system to help interpret testing in the ESF; (2) develop a three-dimensional DFN model to define as precisely as possible the flow geometry of the Topopah Spring Tuff to reduce uncertainty in understanding and predicting flow parameters and behavior; (3) derive directional-permeability distributions for fracture networks at different scales; (4) determine, if possible, at what scale the rock functions as an equivalent continuum; and (5) calculate water flux in a two-phase flow, fractured-rock system. This study will help characterize the fracture geometry and flow system, and the results can be used to help finalize input

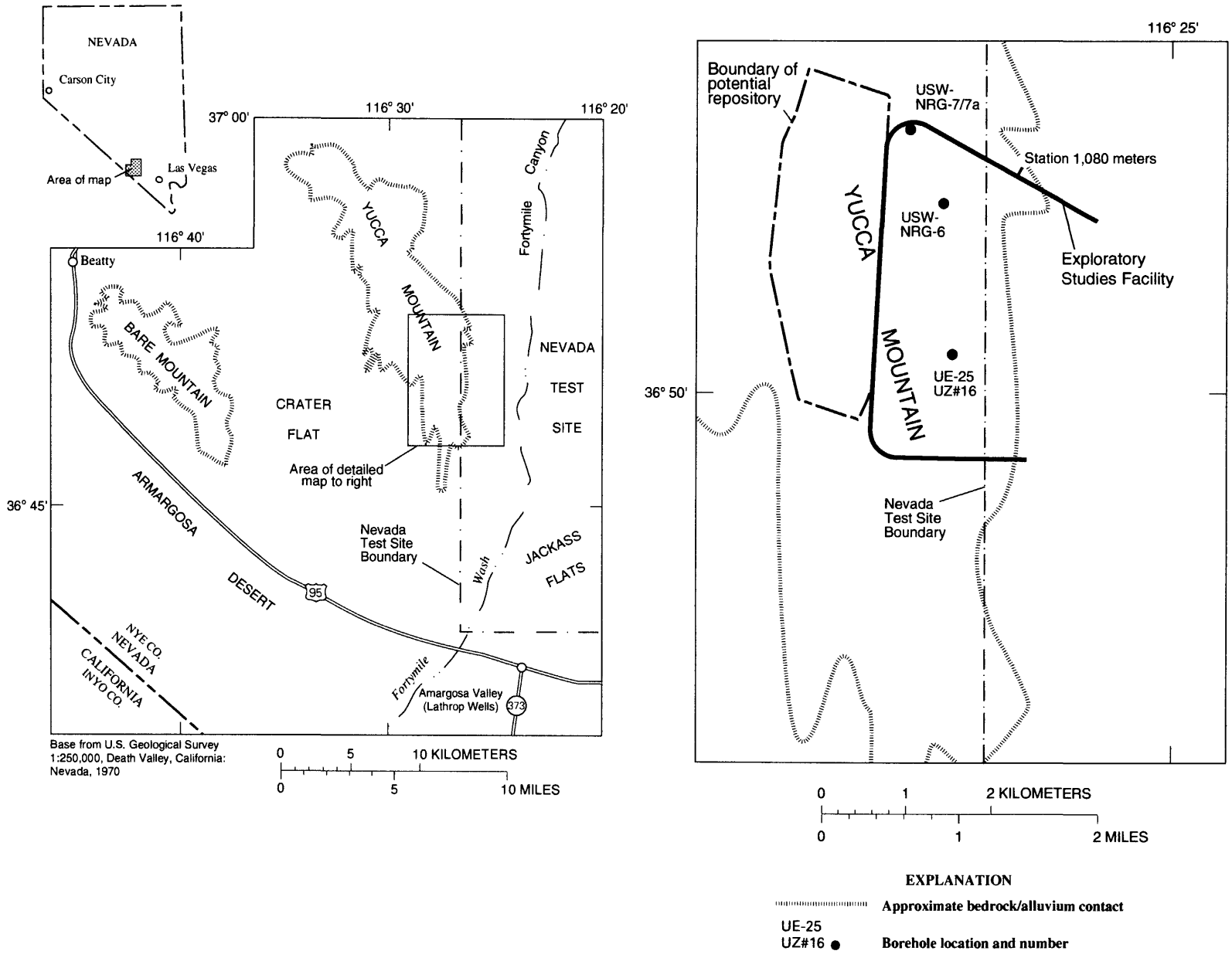

Figure1. Location of study area, including the Exploratory Studies Facility.

parameters and locate potential fast pathways for a model of the site as described in Wittwer and others (1993).

Field and laboratory data and information are used to develop an understanding of the geologic and hydrogeologic system. This study focused on a basic understanding of the geologic framework including fracture genesis and geometry. This information was used to interpret ambiguous results of the flow modeling and field testing. Also, numerical simulations of saturated flow through the framework contributed to a better understanding of the geologic framework and the fracture geometry for the Topopah Spring Tuff, but also can be used for other stratigraphic units.

Acknowledgments

Thanks are extended to Peter Wallmann (deceased) and Paul R. La Pointe, Golder Associates, Redmond, Washington, for their assistance in deciphering the FRACMAN modeling code, and for their helpful discussions on modeling fracture networks.

GEOLOGIC SETTING

Structure

The Yucca Mountain area is approximately 140 kilometers (km) northwest of Las Vegas, Nev., (fig 1). The area consists of a thick sequence of carbonate and clastic rocks of Paleozoic age unconformably overlain by ash-fall and ash-flow tuffs of Miocene age. This volcanic sequence is about 1.5 km thick in the southern part of the area and thickens to about 1.8 km in the northern part. Gravity maps of the area (Snyder and Carr, 1984) can be interpreted to indicate a northeast-southwest thickness trend that thins from north to south. The source of the volcanic rock is thought to be the Timber Mountain-Oasis Valley caldera complex, several kilometers north of the Yucca Mountain area (Spengler and Fox, 1989).

The tuffs at Yucca Mountain may be highly fractured (in terms of the number of fractures per rock volume) because the area is located in a complex tectonic and structural terrain. The terrain is characterized by locally restricted, basin-related extensional tectonics controlled by imbricate faults (Dennis O'Leary, U.S. Geological Survey, written commun., 1995) and a history of repeated movement over geologic time.

There is no single structural and tectonic model of the Yucca Mountain area that is widely accepted. There are many complexities and enigmatic relations in the area that prevent a clearly defined model. Carr (1984) described most of the features that probably affect the overall tectonism and structure of the area. Dennis O'Leary (U.S. Geological Survey, written commun., 1995) indicated that the Yucca Mountain area is not a discrete tectonic block because there are no major bounding faults that define the mountain. Instead, the mountain is a series of block-faulted drapes of volcanic rocks of Miocene age. The faults consist of three fundamental groups: one group propagated upward from underlying Paleozoic units, although little is known about the structural complexity of this group; another group is a surficial population that reflects failure and movement of the volcanic sequence; and the last group is minor faults that occur along penecontemporaneous zones of weakness caused by cooling, degassing, and other diagenetic alterations of the volcanic rock.

In general, exposed rocks at Yucca Mountain form 5- to 15-degree (°) east-dipping blocks separated by down-to-the-west normal faults that have offsets of a few meters to several hundred meters (Scott and Bonk, 1984; Frizzell and Shulters, 1990). Extension faulting probably began prior to the deposition of the Topopah Spring Tuff (Scott, 1990) and continued throughout the deposition of the Topopah Spring Tuff. Faults that trend north-south have dip-slip movement and possibly a minor component of strike-slip displacement (O'Neil and others, 1992). Northwest-southeast-trending faults have right-lateral movement similar to the movement mapped in the Walker Lane structural zone (King, 1975; Wright, 1976). Northeast-southwest-trending faults have left-lateral movement similar to movement in the Spotted Range-Mine Mountain structural zone (Carr, 1984).

Fractures

Because there is no widely accepted regional tectonic and structural model of the Yucca Mountain area, the origin of fracturing is speculative. Except for localized areas and at the surface, similar stresses and

strains have been transmitted over the entire Yucca Mountain area, which means that, spatially, fracture orientations probably do not change substantially. As a result, the region that was simulated was treated as spatially homogeneous.

The chronological sequence of fracture sets is not clearly defined. There is debate whether fracture sets form separately under tension (Don Sweetkind, U.S. Geological Survey, written commun., 1995) or as conjugate sets. However, based on detailed fracture mapping of pavements and uncleared areas, Don Sweetkind (U.S. Geological Survey, written commun., 1995) indicated that, despite ambiguities, a probable chronological sequence of fracture formation can be determined. The sequence starts with cooling joints that formed contemporaneously with deposition and diagenetic alteration of the ash-flow and ash-fall tuffs. Next in the sequence are the tectonic fractures; the north-south-trending fractures formed first, followed by the northwest-southwest-trending fractures, and then by the northeast-southwest-trending fractures. A few east-west-trending fractures may be a result of unloading and may have formed last. If these fractures are unloading features, then the fractures would not be present at depth.

Cooling joints have been mapped and described in the Yucca Mountain area by Barton and others (1993) and Throckmorton and Verbeek (1995), although their origin and characteristics are speculative. Mapping has been limited to parts of the total stratigraphic section. Cooling joints were not defined as a distinct fracture set because (1) the percentage of cooling joints to tectonic fractures is small; (2) distinction of cooling joints from tectonic fractures is not always definitive; and (3) orientations of cooling joints mapped in the ESF can be included in the tectonic sets.

The continuation of fractures between subunits of the Topopah Spring Tuff is not generally known. Qualitative observation of the few contacts in outcrop and in the ESF indicates some throughgoing fractures between subunits. The continuation of fractures between the Topopah Spring Tuff and other continuous stratigraphic units also is generally not known. Don Sweetkind (U.S. Geological Survey, written commun., 1995) indicated that in the overlying nonweled Paintbrush Group and nonwelded (PTn) vitric units, fractures are predominantly stratabound. However, there probably are a number of fractures that connect the top of the welded Topopah Spring Tuff to the lower part of the overlying moderately welded vitric subzone of the PTn.

Numerous faults in the area have been mapped (Scott and Bonk, 1984) and could be either potential fast pathways or barriers to water and air flow and radionuclide transport (Montazer and Wilson, 1984). Because hydraulic parameters of the faults in the area have not been determined and because the relation of faults to fractures has not yet been determined, this preliminary study does not include faults as part of the connectivity of the system.

Stratigraphy

Stratigraphy of the Topopah Spring Tuff at Yucca Mountain is relatively simple and uncomplicated. The vertical sequence is probably the result of one ash-flow cycle separated by unconformities at the top and bottom. A simplified cycle consists of an asymmetric bulk-density profile of non-welded to moderately welded tuff at the top and bottom of the stratigraphic unit and welded to densely welded tuff in the middle. The unit has a maximum thickness of about 350 meters (m) (Buesch and others, 1996) and at Yucca Mountain averages about 275 m. Hydraulic properties are laterally consistent with occasional local stratigraphic anomalies (Rautman and Flint, 1992).

A basic depositional model for ash-flow tuffs that is used in this study is from Riehle (1973), Riehle and others (1995), and Buesch and others (1996). Computed compaction, density, and porosity profiles indicate the tuffs are asymmetric and have a gradual slope in the upper part and a fairly sharp base. Local variations from this general profile may occur because of temperature or chemistry anomalies. The middle parts of the tuffs are welded to densely welded and have porosities of 0 to 5 percent. The upper and lower parts are nonwelded to slightly welded and have porosities as high as 45 percent. Riehle and others (1995) described the Matahina Ignimbrite in New Zealand, which has characteristics similar to the Topopah Spring Tuff. Based on density profiles, the Matahina Ignimbrite was divided into three members. The basal member is thin and devitrified and includes a vitrophyre layer. The middle member is a thick, devitrified section and the upper part of the member consists of a vapor-phase crystallization. The upper member is a thin vapor-phase crystallization layer.

The Topopah Spring Tuff has a similar profile as described by Buesch and others (1996).

The Topopah Spring Tuff can be divided into several informal stratigraphic units based on internal texture, percent of phenocrysts, presence or absence of lithophysae, and degree of welding (Buesch and others, 1996) (fig. 2).

DISCRETE FRACTURE-NETWORK MODEL

Initial Network

This study used the forward modeling approach of FRACMAN (Dershowitz and others, 1994) to develop a three-dimensional DFN model of the Topopah Spring Tuff. During the development of the DFN, alternative probabilistic fracture models were evaluated using field measurements. Field data were obtained from detailed line surveys (DLS) in the ESF and from packer tests in boreholes. The data were analyzed to estimate fracture length, orientation, location, and transmissivity. Models for these parameters were used to create a stochastic DFN. The simulated network then was analyzed for specific geometric configurations including connectivity, spatial configuration, and rock-block sizes. The network also could be discretized into finite elements to solve flow equations to calculate flux and permeability.

Data Collection

Fractures

Primary sources for fracture data were DLS of the ESF (station 1,080 to station 4,000 m) and a limited number of full periphery maps for the ESF (table 1).

<table>
<tr><th colspan="4">Lithostratigraphic units</th><th>Hydrogeologic units</th><th>Fracture subunits</th></tr>
<tr><td rowspan="15">Topopah Spring Tuff (Tpt)</td><td rowspan="5">Crystal-rich</td><td rowspan="3">Vitric</td><td>Nonwelded</td><td rowspan="5">Topopah Spring welded 1 (TSw1)</td><td rowspan="3">FSU1</td></tr>
<tr><td>Moderately welded</td></tr>
<tr><td>Densely welded</td></tr>
<tr><td>Nonlithophysal</td><td rowspan="4">--</td></tr>
<tr><td>Lithophysal</td><td>FSU2</td></tr>
<tr><td rowspan="10">Crystal-poor</td><td>Upper lithophysal</td><td rowspan="4">Topopah Spring welded 2 (TSw2)</td></tr>
<tr><td>Middle lithophysal</td><td>FSU3</td></tr>
<tr><td>Lower lithophysal</td><td rowspan="2">Hackly fractured</td></tr>
<tr><td rowspan="2">Nonlithophysal</td><td>FSU4</td></tr>
<tr><td>Columnar</td></tr>
<tr><td rowspan="3">Vitric</td><td>Densely welded</td><td>Topopah Spring welded 3 (TSw3)</td><td>FSU5</td></tr>
<tr><td>Moderately welded</td><td rowspan="3">Calico Hills nonwelded 1 (CHn1)</td><td rowspan="3">--</td></tr>
<tr><td>Nonwelded</td></tr>
<tr><td>Pre-Tpt bedded</td><td>--</td><td>--</td></tr>
</table>

Figure 2. Stratigraphic chart for the Topopah Spring Tuff. Modified from Scott and Bonk (1984), Ortiz and others (1985), and Buesch and others (1996). Subunits FSU 4 and FSU 5 were not part of this study.

Table 1. Field-data source

[Q = qulaified; NA = not available; ESF = Exploratory Studies Facility]

Data-tracking number (DTN) accession number	Title	Q status
GS960408314224.002 NA	Detailed line survey, ESF, stations 10 to 18	Q
GS960608314224.006 NA	Detailed line survey, ESF, stations 18 to 26	Q
GS960608314224.007 NA	Detailed line survey, ESF, stations 26 to 30	Q
GS960708314222.008 NA	Detailed line survey, ESF, stations 30 to 35	Q
GS960808314224.011 NA	Detailed line survey, ESF, stations 35 to 40	Q
GS960408314224.003 NA	Full periphery maps, ESF, stations 10 to 18	Q
GS960708314224.009 NA	Full periphery maps, ESF, stations 18 to 26	Q
GS950108312232.002 MOL.19930524.0066	In-situ pneumatic testing of boreholes. Borehole USW NRG-6	Q
GS950108312232.001 MOL.19950524.0114	In-situ pneumatic testing of boreholes. Borehole USW NRG-7/7a	Q
GS940108312232.003 MOL.19941108.0003	In-situ pneumatic testing of boreholes. Borehole UE-25 UZ-16	Q
MOL.19941108.0004		Q
MOL.19941108.0005		
MOL.19941108.0006		
MOL.19941108.0007		
GS950708312232.006 MOL.19960229.0028	In-situ pneumatic testing of boreholes. Borehole UE-25 UZ-16	
GS950208312232.003 NA	In-situ water-potential measurements, USW NRG-7/7a and USW NRG-6	Q
GS951108312232.008 NA		
GS960308312232.001 NA		
GS960808312232.004 NA		

Fracture attributes that were used in the analysis from the DLS were orientation, length, fracture station position, and occurrence of calcite in fractures. Full periphery maps for the ESF (right wall panel only) were used (station 1,000 to station 2,600 m) to analyze fracture intensity, including the number of fractures per meter and total fracture length per square meter. Only the right wall panel was used in the calculation and calibration because the crown panels often had missing data because of steel lagging or other obstructions. These intensity measurements were used to condition the simulated network.

Well Tests

The USGS has developed methods and equipment to provide estimates of in-situ air-permeability values in fractured rock (LeCain, 1995). Air-permeability testing data from two vertical boreholes (USW NRG-6 and USW NRG-7/7a, table 1) were used to determine a transmissivity distribution and frequency

of conductive fractures, as described in the section on the conductive fracture model. Each borehole was tested using approximately 4.3-m-long packer intervals. The packed-off interval was injected with air to a steady-state flow condition using different flow rates. Injection was stopped and a recovery curve was evaluated (G.D. LeCain, U.S. Geological Survey, written commun., 1996). Measured air-permeability distributions for the boreholes are shown in figures 3 and 4. By visual inspection the histograms show very rough lognormal distribution with geometric means for USW NRG-6 of 9.32×10^{-8} meters squared (m^2) and for USW NRG-7/7a of 3.36×10^{-6} m^2.

Data Analysis

Fracture Intensity

There are many methods for measuring fracture intensity, but the preferred method in this study was fracture area to rock volume, or P32, because it is scale independent. This method is different from measuring fracture density, which is the total number of fractures per volume and is scale dependent. Fracture density means little in terms of connectivity of the DFN, because there is no length or size factor involved.

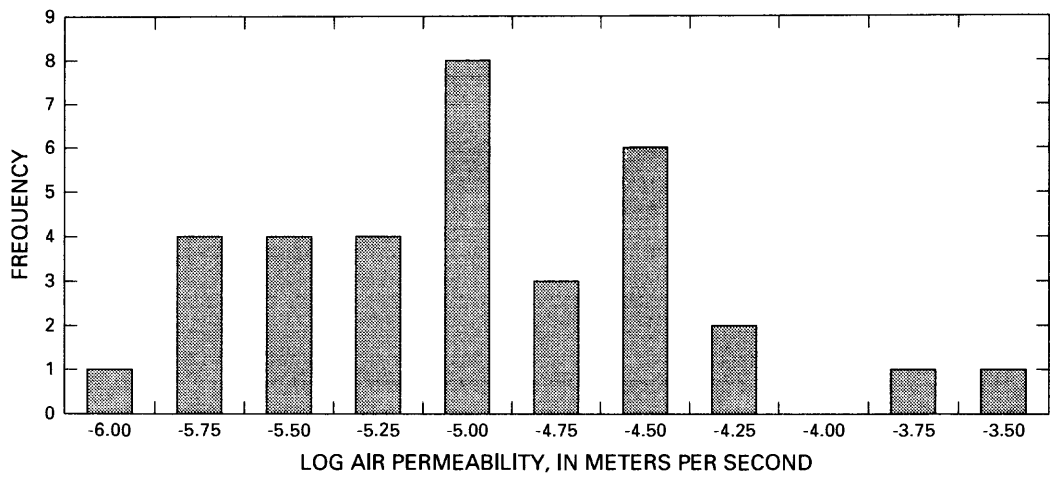

Figure 3. Air permeability, borehole USW NRG-6, Topopah Spring Tuff.

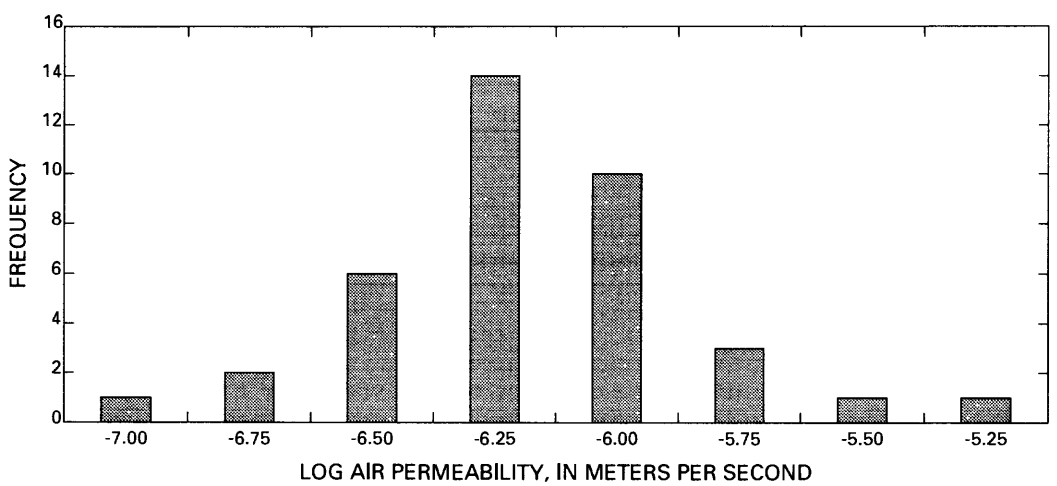

Figure 4. Air permeability, borehole USW NRG-7/7a, Topopah Spring Tuff.

The P32 intensity [square meter per cubic meter (m^2/m^3)] cannot be directly measured. However, P21 (trace length per rock surface area, m/m^2) and P10 (number of fractures per meter, or λ) can be measured. Both parameters have the same units per meter (m^{-1}) and are linearly related for a given volume of rock, although P10 is scale dependent and P21 is scale independent. P10 can be calculated from line samples or boreholes, whereas P21 can be calculated from the full periphery maps from the ESF and is the more robust calculation of the two. $P21_{SIM}$ and $P10_{SIM}$ (SIM meaning simulated) were calculated from two-dimensional traceplanes and line surveys inserted into a simulated network that had the same length or area and orientation as the mapped traceplanes and lines. The intensity of the fracture simulation, $P32_{SIM}$ was adjusted until $P21_{SIM} = P21_{MAPPED}$ (MAPPED meaning recorded fracture parameters from the ESF) and when $P10_{SIM}$ was equal to or almost equal to $P10_{MAPPED}$. $P10_{SIM}$, however, was only a general indicator of the fit, because it is scale dependent. Calibration of the simulated DFN was done by comparing simulated and mapped fracture intensities. The simulated intensity results are listed in table 2 and the mapped intensity values are listed in table 3. The P21intensity measurement from the simulation results matched well with the mapped results. However, the P10 simulated intensity measurement did not match the mapped measurement. Different truncation values used in the DLS and the full periphery mapping may account for the discrepancy. Regardless of what type of input parameter adjustments were made, the P21 and the P10 of the simulated and the mapped would not match. Because the P21 match is the more robust of the two and is scale independent, and P10 is only a general indicator of conditioning fit, and because the difference between the P10 mapped and simulated results was not large, the simulated network may represent the real fracture network. A visual comparison made between simulated and mapped fractures is shown in figures 5 and 6. The comparison is for fracture subunits FSU 1 and FSU 2 (see below for explanation of subunits), showing different intensities for different parts of a full periphery map in the ESF. Because the simulated network represents only one realization the match was not perfect, but is believed to be acceptable given the uncertainties that in producing the realization.

The simulated network was segmented vertically into three layers (FSU 1, 2, and 3). Each subunit has unique characteristics based on differences of intensity, spacing, and rock characteristics. The Topopah Spring Tuff was actually divided into five subunits; however, only the top three subunits had sufficient data to analyze and simulate. The top subunit (FSU 1) is equivalent to the top of the crystal rich-vitric lithostratigraphic unit and the top one-half of the crystal-rich nonlithophysal unit (fig. 2). The middle subunit (FSU 2) is equivalent to the bottom one-half of the crystal-rich nonlithophysal unit and the crystal-rich lithophysal and the crystal-poor upper lithophysal unit. The bottom subunit (FSU 3) is equivalent to the crystal-poor middle nonlithophysal unit and the crystal-poor lower lithophysal unit although a secondary division exists at the base of the middle nonlithophysal unit. Because the tunnel boring machine did not penetrate the lower nonlithophysal unit, this unit was not included in the analysis.

Fracture frequencies and orientations with distance along the ESF are shown in figure 7. The bottom of FSU 1 (top of FSU 2) is placed at station 1,331 m because of a change in fracture spacing from an average of 0.5 to 1.0 m and an apparent change in fracture orientation. The bottom of FSU 2 (top of FSU 3) is placed at station 2,720 m because of a change in fracture spacing, because geophysical logs indicate major changes in rock properties, and because of a major stratigraphic break between hydrostratigraphic units TSw1 and TSw2 (fig. 2). The bottom of FSU 3 was not reached in the ESF and only data to station 4,000 m were available at the time of analysis. Although there was a major intensity change at station 3,800 m, where fracture spacing was from about 0.3 m to 1.0 m, FSU 3 was not further divided because of a lack of data availability beyond station 4,000 m. Subunits FSU 1, 2, and 3 were stacked (with 10 m of overlap) to form the complete DFN.

Orientation

Mapped orientation data were from ESF DLS. The data from the ESF were analyzed in four parts: a northwest-oriented segment (north ramp), a north-south-oriented segment (middle ramp), a curved segment that links the first two segments, and combined segments (fig.1). The data indicate that orientations were biased against fractures that parallel or nearly parallel straight-line parts of the ESF. The northwest segment has few northwest-oriented fractures (fig. 8). Yet, from mapping of the overlying Tiva

Table 2. Fracture intensities calculated from simulated data, Topopah Spring Tuff

[FSU 1 is equivalent to the top of the crystal-rich vitric lithostratigraphic unit and the top one-half of the crystal-rich nonlithophysal unit; FSU 2 is equivalent to the bottom one-half of the crystal-rich nonlithophysal unit and the crystal-rich lithophysal and the crystal-poor upper lithophysal unit; FSU 3 is equivalent to the crystal-poor middle lithophysal unit and the crystal-poor lower lithophysal unit; no explicit data exists for underlying units. std. dev., standard deviation]

Fracture subunit	Number of intersections per square meter	Number of fractures per square meter P20	Fracture length per square meter P21	Number of fractures per meter P10	Fracture area per rock volume (square meter per cubic meter)	
					Inital network $P32_I$	Connected network $P32_C$
FSU 1					1.89	0.433
Mean	0.492	0.544	1.293	1.339		
Std. Dev.	0.109	0.042	0.109	0.105		
FSU 2					0.658	0.49
Mean	0.041	0.144	0.374	0.355		
Std. Dev.	0.017	0.026	0.07	0.065		
FSU 3					1.89	0.433
Mean	0.492	0.544	1.293	1.339		
Std. Dev.	0.109	0.042	0.109	0.105		

Table 3. Fracture intensities calculated from Exploratory Studies facility, mapped data, Topopah Spring Tuff

[FSU 1 is equivalent to top of the crystal-rich vitric lithostratigraphic unit and the top one-half of the crystal-rich nonlithophysal unit; FSU 2 is equivalent to the bottom one-half of the crystal-rich nonlithophysal unit and the crystal-rich lithophysal and the crystal poor upper lithophysal unit; FSU 3 is equivalent to the crystal-poor middle lithophysal unit and the crystal-poor lower lithophysal unit; no explicit data exists for underlying units]

Fracture subunit	Fracture length per square meter P21	Number of fractures per meter P10
FSU 1	1.22	1.82
FSU 2	0.41	0.53
FSU 3	1.22	1.82

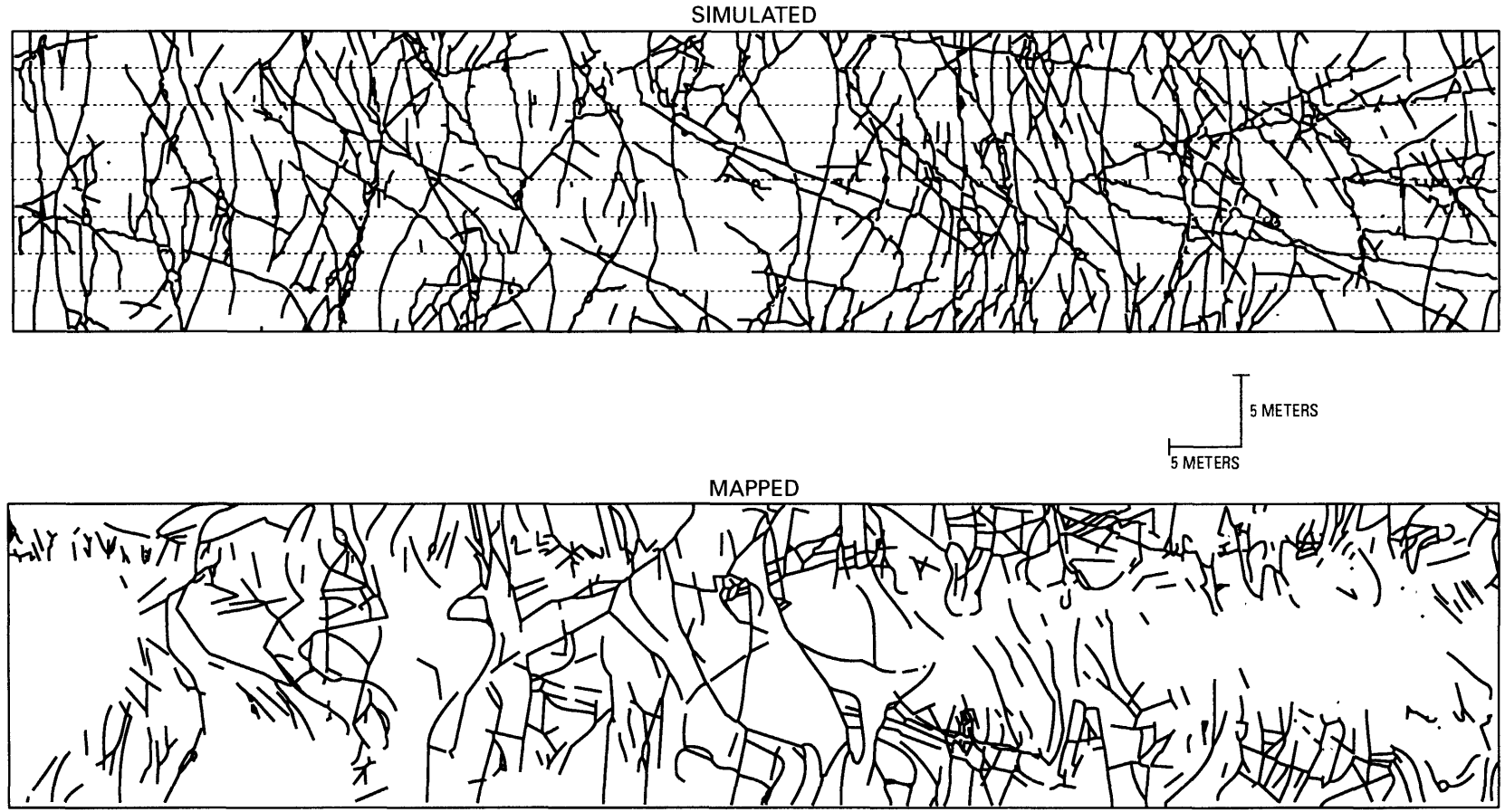

Figure 5. Fractures displayed in a 100-meter-long, unfolded, full periphery map of the Exploratory Studies Facility (tunnel) for fracture subunit FSU 1. Right and left benches on the map edge, with the crown in the center. The simulated tunnel is divided into 8 panels (excluding the invert) seperated by horizontal dotted lines. Blank areas in the mapped display are from either steel lagging or other obstructions to mapping.

Figure 6. Fractures displayed in a 100-meter-long, unfolded, full periphery map of the Exploratory Studies Facility (tunnel) for fracture subunit FSU 2. Right and left benches on the map edge, with the crown in the center. The simulated tunnel is divided into 8 panels (excluding the invert) seperated by horizontal dotted lines. Blank areas in the mapped display are from either steel lagging or other obstructions to mapping.

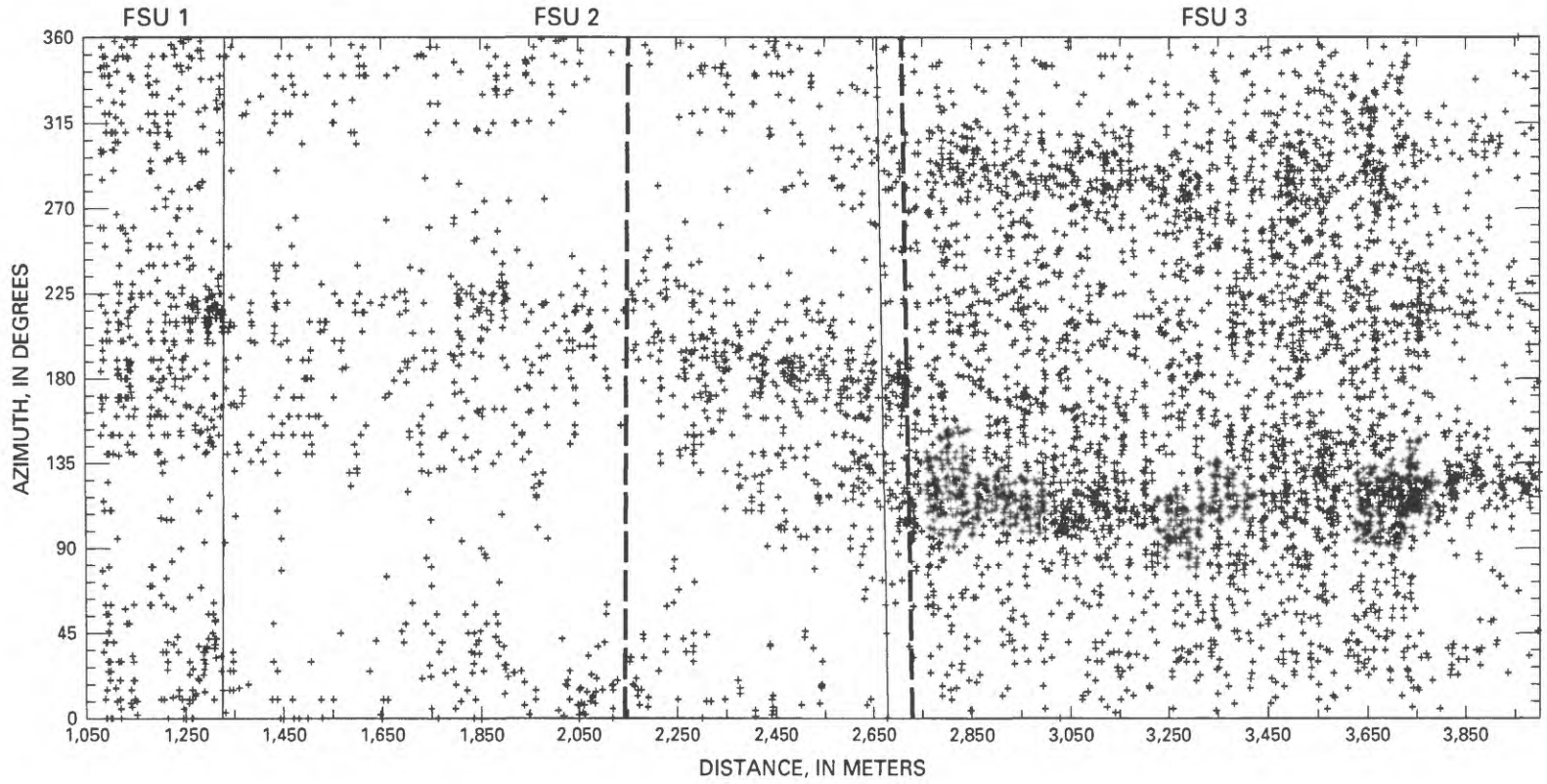

Figure 7. Plot showing fracture azimuth (poles) to distance along Exploratory Studies Facility. Dashed vertical lines bracket the curved segment. Solid vertical lines are fracture subunit (FSU) boundaries.

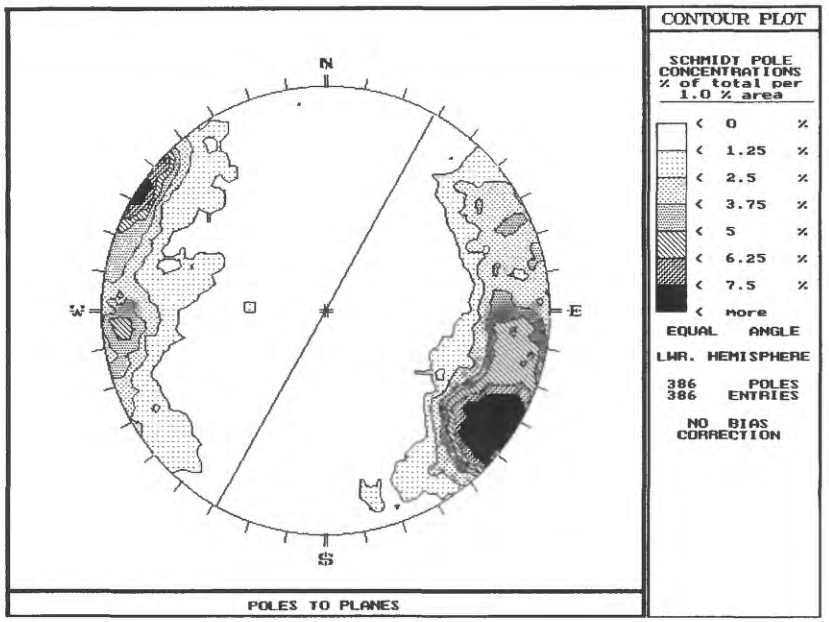

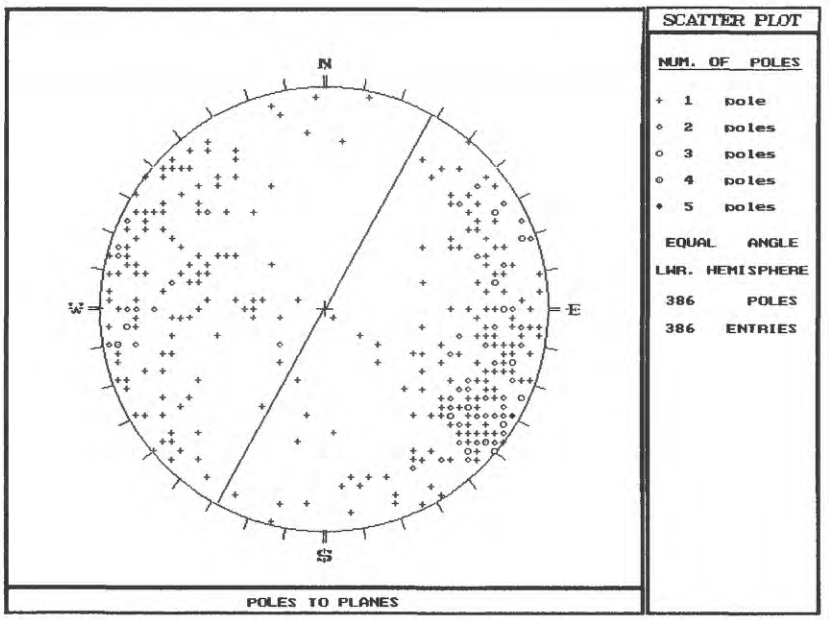

Figure 8. Equal-area Schmidt pole plot showing fractures from the Exploratory Studies Facility northwest segment. Only fractures greater than 1.5 meters in length are plotted. Solid line is pole direction of the Exploratory Studies Facility.

Canyon Tuff and from mapped orientations in the north-south and the curved segment, northwest-oriented fractures are common. Also, there is a bias against north-south oriented fractures that parallel the north-south-oriented ESF (fig. 9). In the northwes-oriented segment there are north-south fractures present. The curved segment (fig. 10) has an orientation similar to the combined segments (fig. 11), indicating that the curved segment is representative of all orientations. The bias also is emphasized in figure 7, which shows the orientations at about 180 and 0° starting to drift at the start of the curve (station 2,200 m) to the end of the curve (station 2,800 m). To correct the bias, Terzaghi corrections (Terzaghi, 1965) were attempted but were unsuccessful. Therefore, fracture orientations from all three segments were combined to eliminate orientation bias. Because the segments were combined, the orientations represented a homogeneous sampling of the modeled area. However, the percent occurrence of orientations from the north-south segment was much greater than the percent occurrences from the northwest and curved segments as shown in figures 12, 13, and 14. Therefore, an equal number of orientations were sampled and made available for model input from each segment.

The combined segment equal-area Schmidt plot (fig. 11) indicated that there were three dominant fracture sets: N.65°W., 85°SW.; N.03°W., 85°W.; and N.33°E., 85°NW. The fracture sets were also listed in order of relative abundance. Although these orientations were not used as simulation input, they do represent a collaboration with fracture orientations in the overlying Tiva Canyon Tuff and with faults mapped in the ESF.

To convert the mapped orientation data into simulation input parameters, techniques were attempted that were similar to the techniques used for the Tiva Canyon Tuff DFN (Anna, 1997; and Anna and Wallmann, 1997) in which mapped fractures were segregated into fracture sets. Numerous attempts were made to define specific fracture sets using spherical distribution techniques and probabilistic pattern recognition (ISIS module in FRACMAN, Dershowitz and others, 1994), but satisfactory statistical confidence levels were never achieved. Therefore, fracture orientations, taken directly from ESF DLS fracture mapping, were bootstrapped (Efron, 1982) into the simulated network in which fracture orientations were simulated directly from the modified DLS and expanded to three-dimensional space. All layers in the simulated network used the same orientation distribution, with only fracture intensity varying vertically.

Size

Data for mapped fracture lengths were from ESF DLS. Lengths ranged from 30 centimeter (cm) (minimum cutoff length) to 22 m. There was no correlation between length and orientation, even though fractures that parallel the ESF had a greater probability of having long lengths. Length histograms for each ESF segment and combined segments (figs. 15 through 18) show a powerlaw, or exponential distribution, except for the curved segment, which shows more of a lognormal distribution. No attempt was made to specifically define the distribution type.

The ESF data were used to estimate an effective fracture radius (or size) from the trace-length distribution using the FRACSYS module in FRACMAN (Dershowitz and others, 1994). Fracture size is related to fracture area per rock volume, and is used as a direct input parameter into developing the three-dimensional fracture-network model. The FRACSYS algorithm allows an initial estimate of the fracture-size distribution and simulates a length distribution. The initial estimate is changed by optimization algorithms until the simulated length distribution matches the mapped length distribution, as long as the matches are within acceptable limits and are for similar sampling areas. The optimized estimate then is used as the fracture-size distribution. This process is used to analyze each subunit of the network. This approach helps eliminate censoring and truncation bias.

Conductive Network

An objective in modeling discrete fractures is to identify and map fractures that are connected to each other. The initial simulated fracture network had numerous small fractures that were unconnected and did not contribute to the flow system. Therefore, a conductive or connected fracture network that was modified from the initial simulated network was developed based on an approach developed by Osnes and others (1988) and incorporated into OXFILET, a module in FRACMAN (Dershowitz and others, 1994). The approach uses well or borehole tests to determine conductive versus nonconductive fractured intervals.

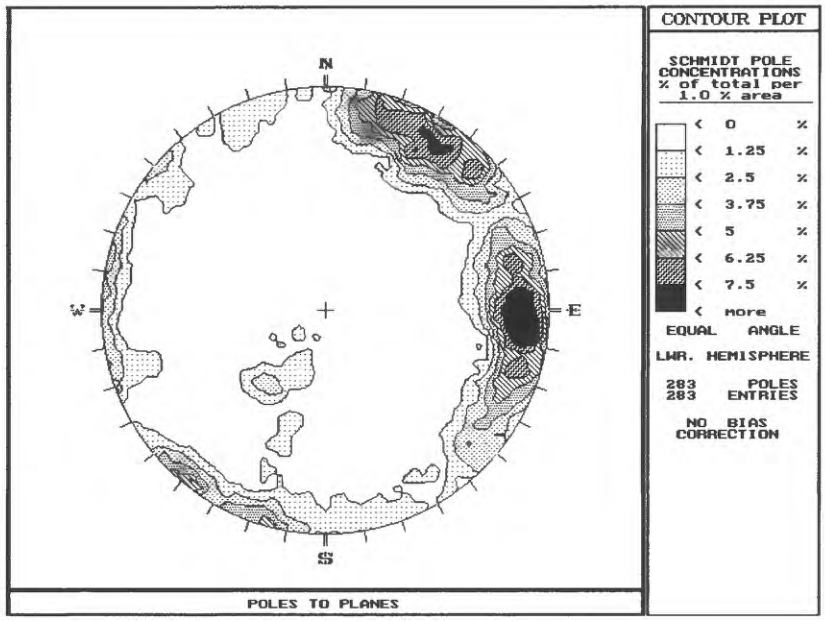

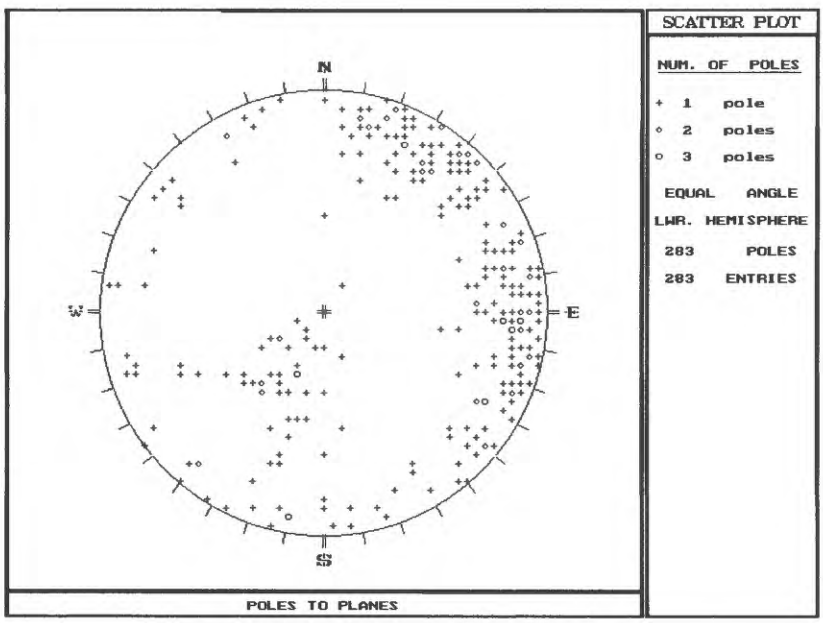

Figure 9. Equal-area Schmidt pole plot showing fractures from the Exploratory Studies Facility curved segment. Only fractures greater than 1.5 meters in length are plotted.

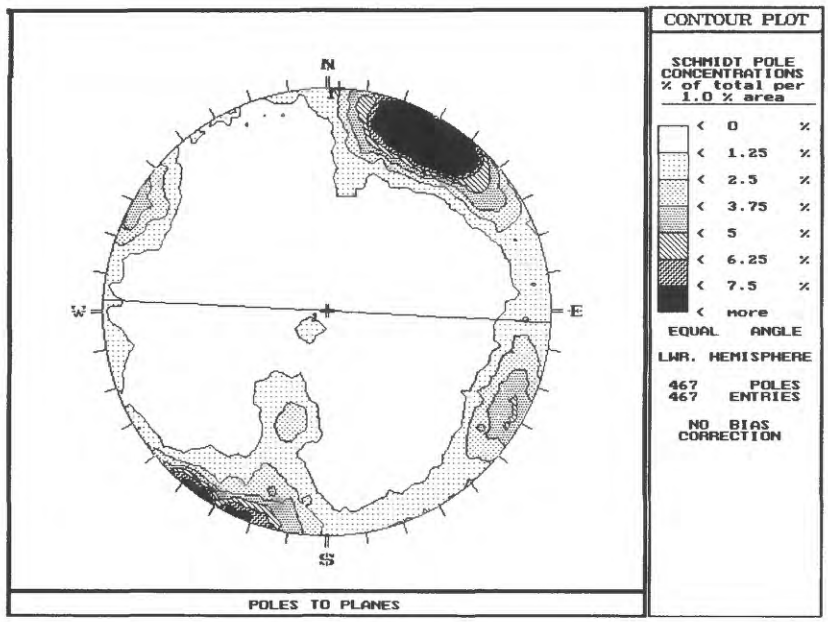

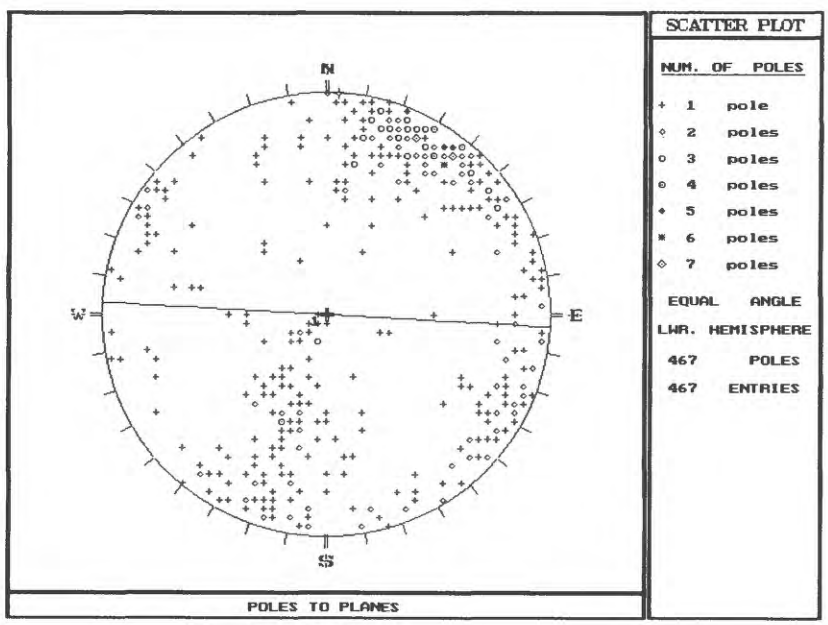

Figure 10. Equal-area Schmidt pole plot showing fractures from the Exploratory Studies Facility north-south segment. Only fractures greater than 1.5 meters in length are plotted. Solid-line is pole direction of the Exploratory Studies Facility.

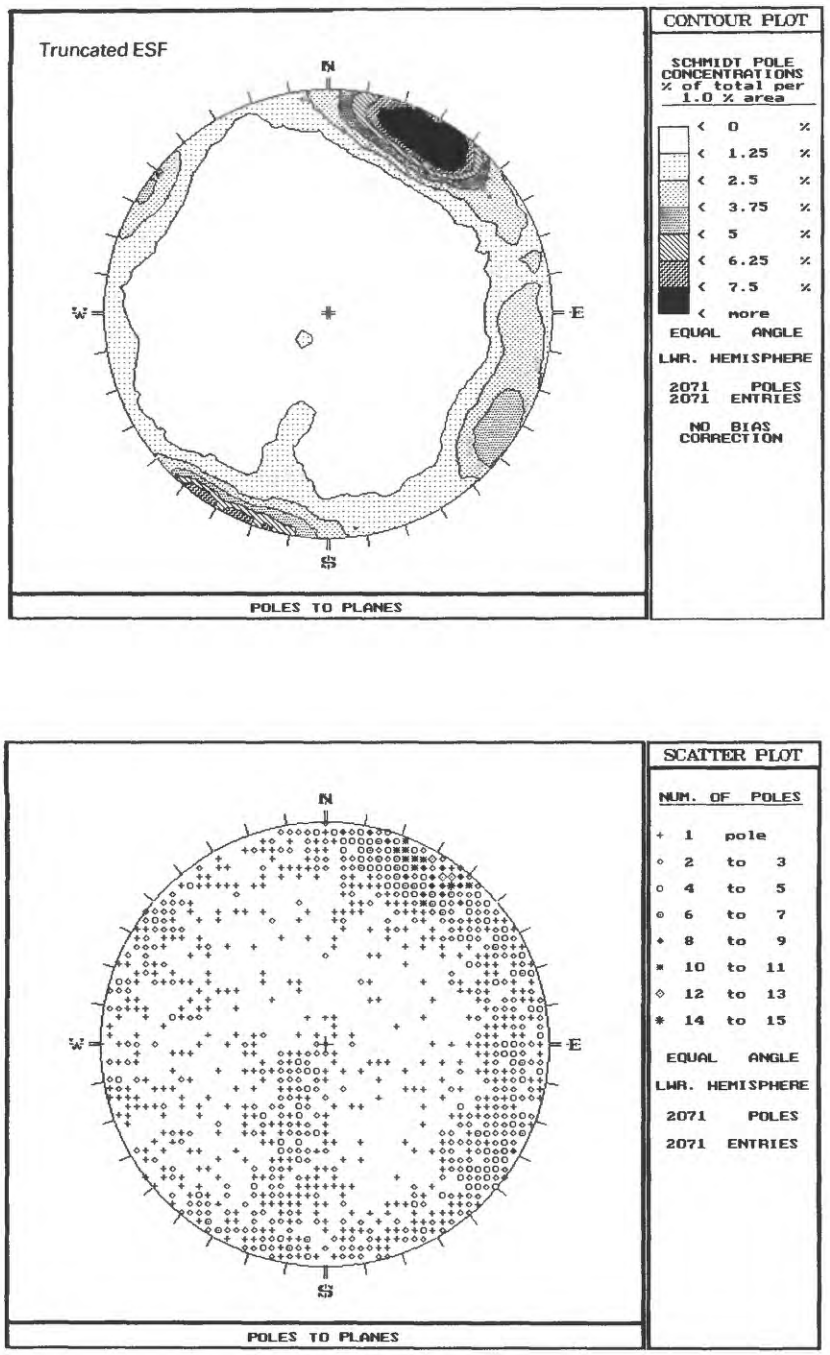

Figure 11. Equal-area Schmidt pole plot showing fractures from the Exploratory Studies Facility combined segments. Only fractures greater than 1.5 meters in length are plotted.

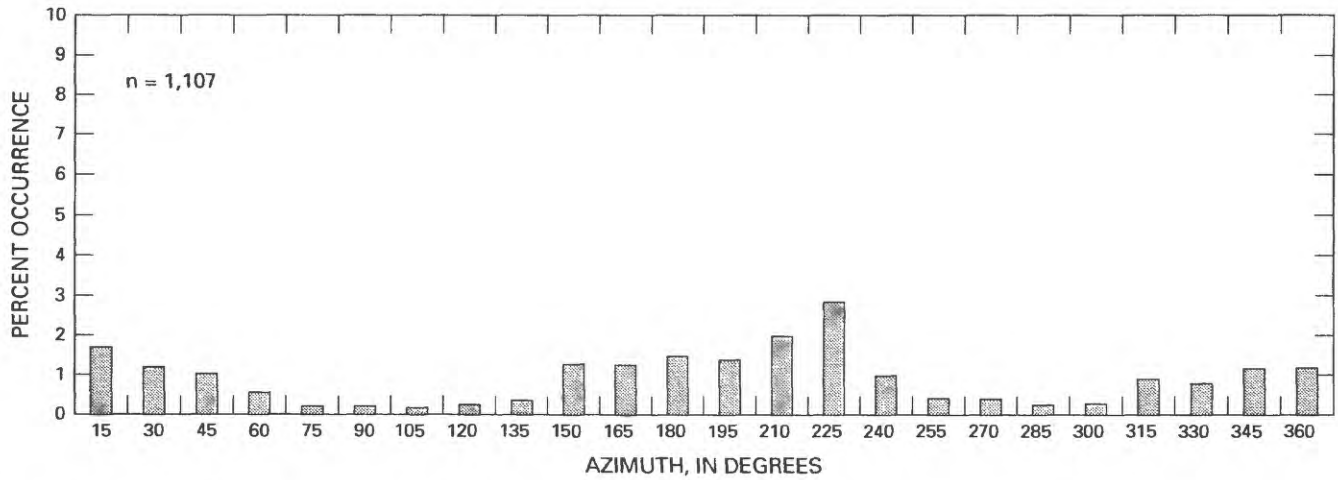

Figure 12. Percent occurrence of fracture orientation of northwest segment to all Exploratory Studies Facility Segments.

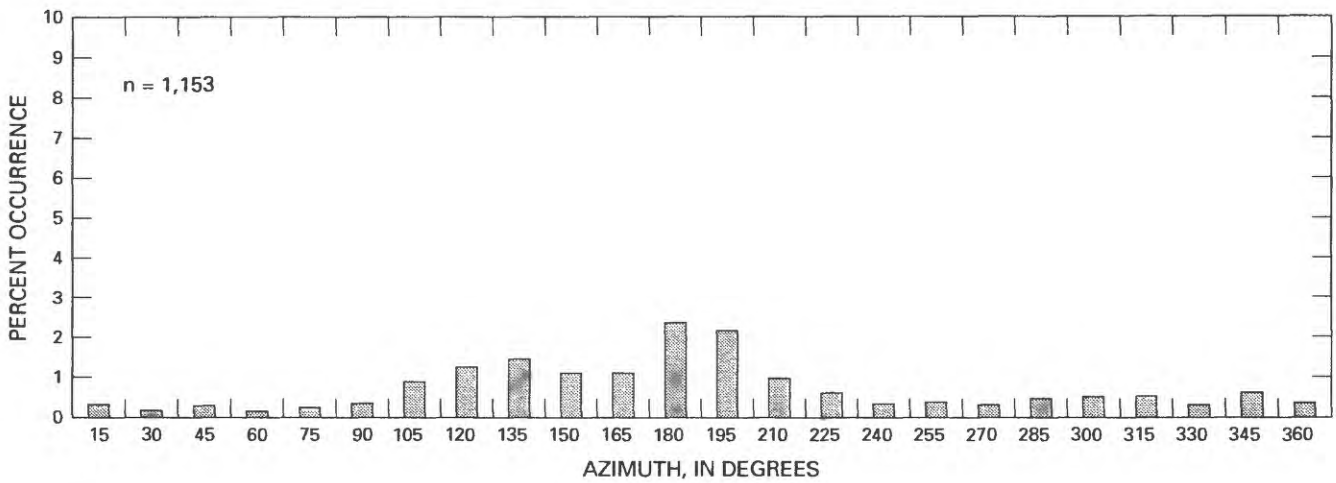

Figure 13. Percent occurrence of fracture orientation of curved segment to all Exploratory Studies Facility Segments.

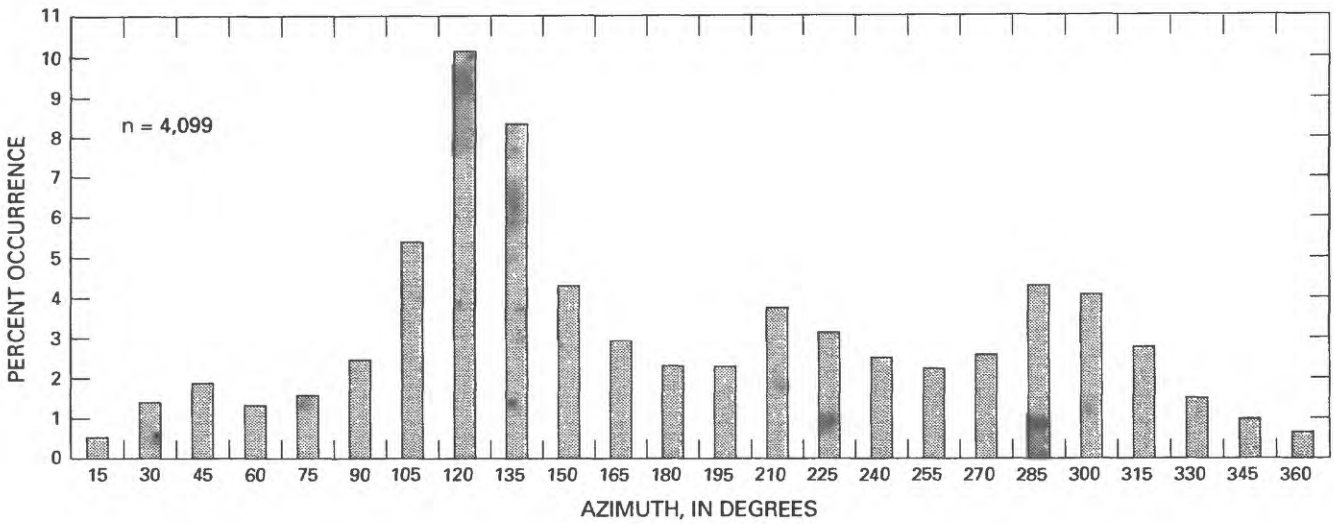

Figure 14. Percent occurrence of fracture orientation of north-south segment to all Exploratory Studies Facility Segments.

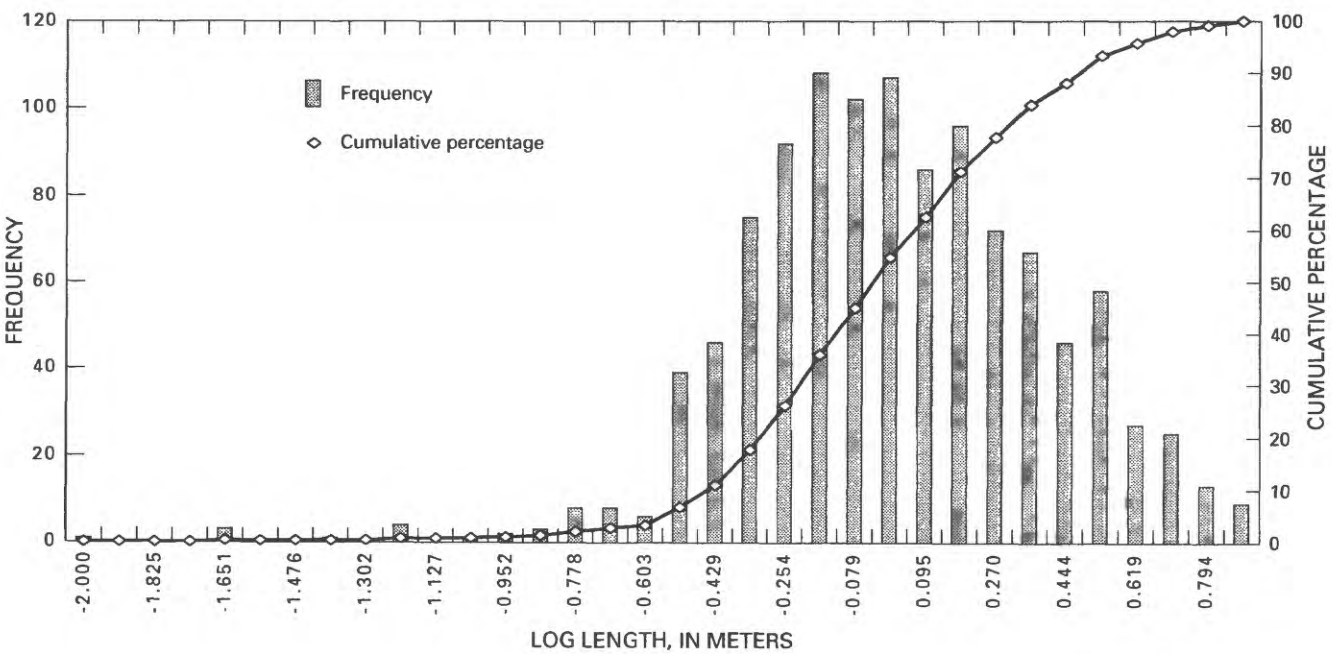

Figure 15. Fracture length, Topopah Spring Tuff, Exploratory Studies Facility, northwest segment.

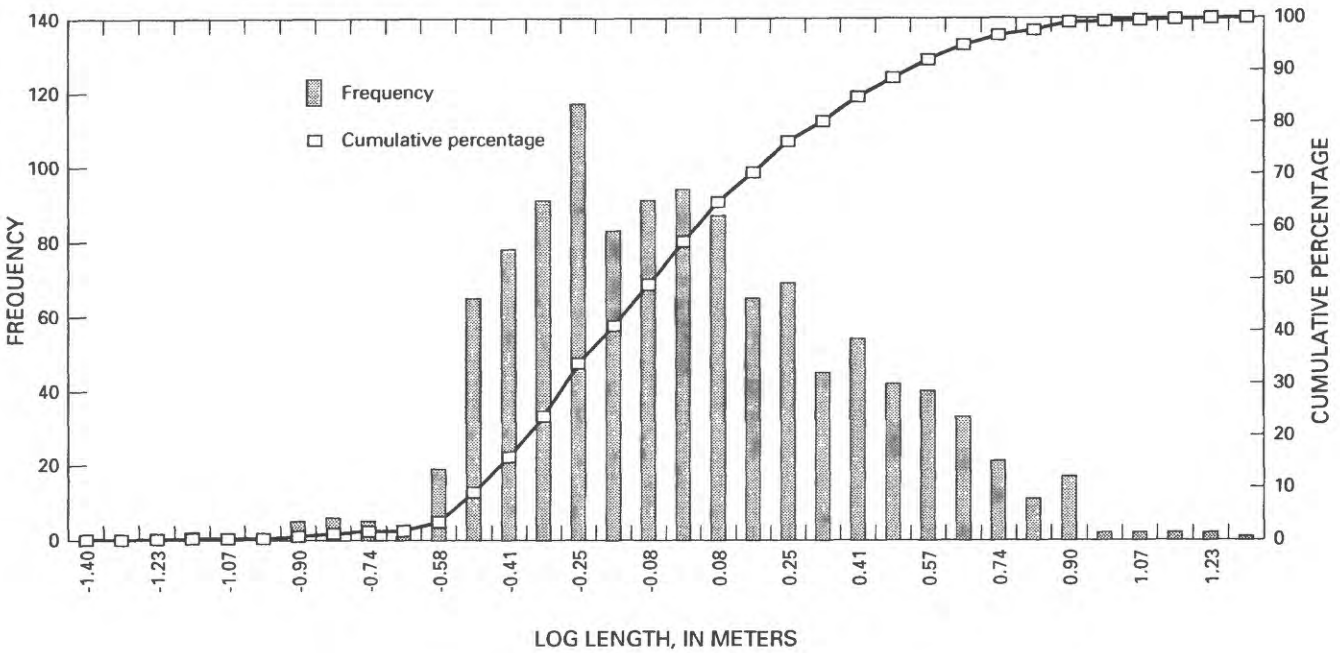

Figure 16. Fracture length, Topopah Spring Tuff, Exploratory Studies Facility, curved segment.

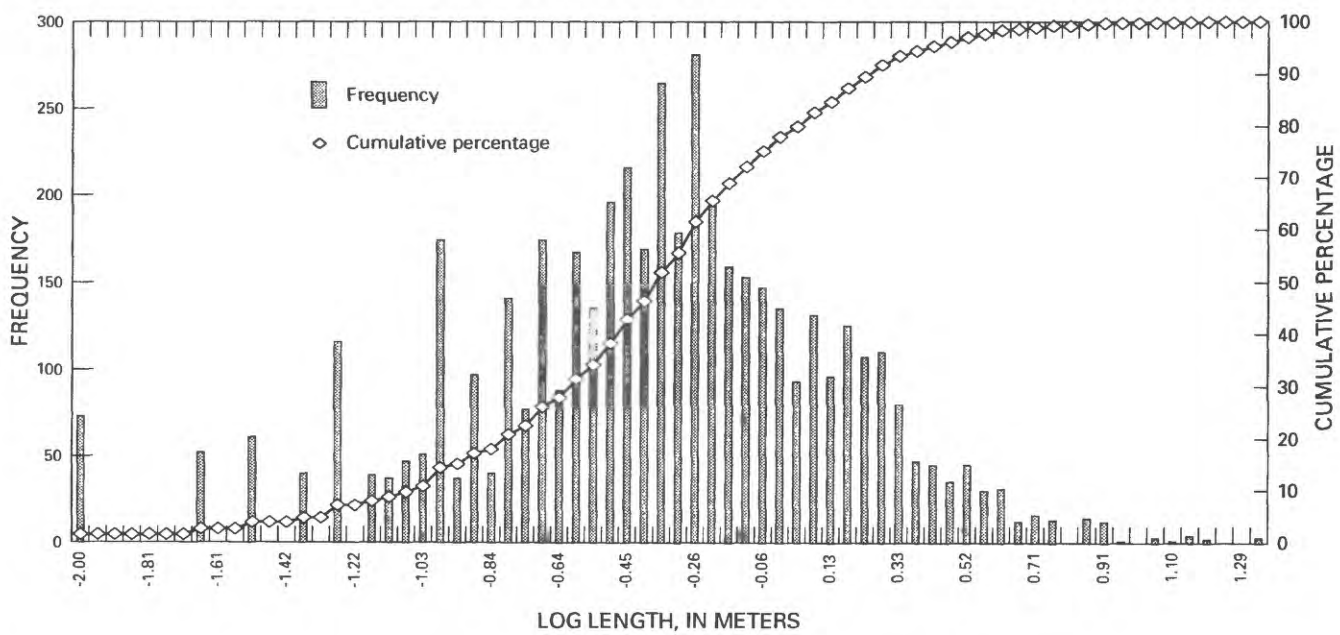

Figure 17. Fracture length, Topopah Spring Tuff, Exploratory Studies Facility, north-south segment.

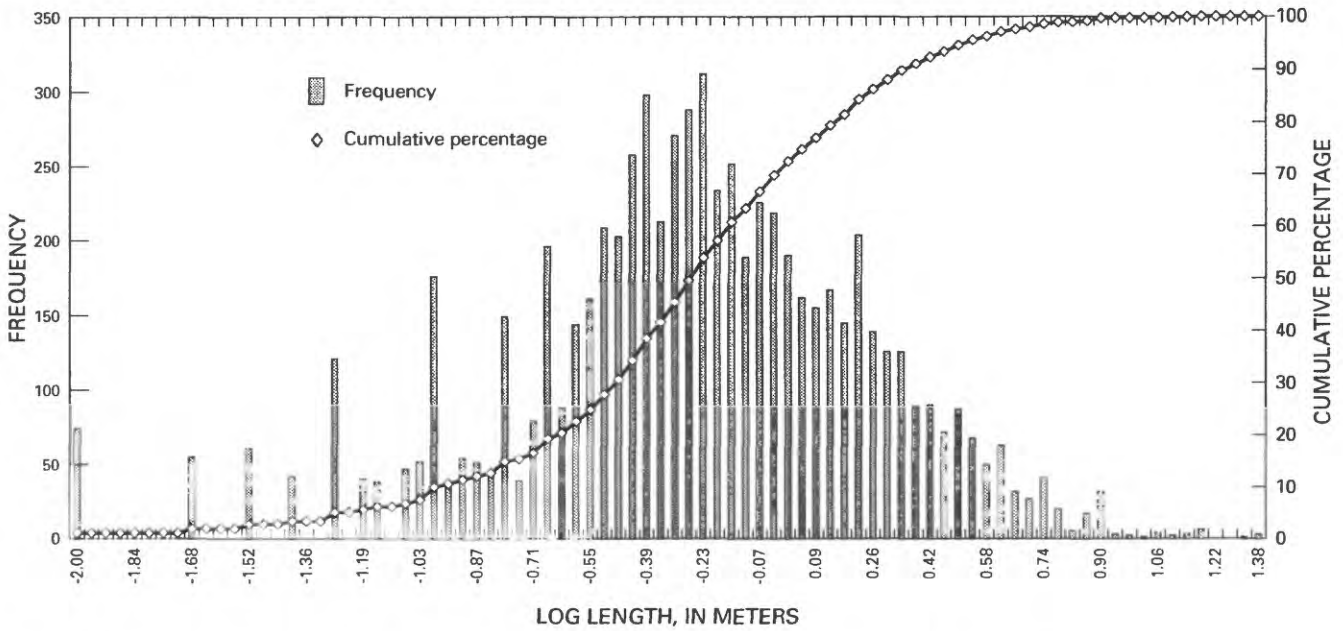

Figure 18. Fracture length, Topopah Spring Tuff, Exploratory Studies Facility, combined segments.

The analysis assumes that the net transmissivity of a packed-off zone is equal to the sum of the transmissivities of the conductive fractures that intersect the packed-off zone for a given initial frequency, λ_i (number per meter) and a minimum (or nonconductive) transmissivity. Packer interval transmissivities are simulated for different frequencies and transmissivity distributions until a statistically valid match is made between the field and simulated transmissivity distributions (table 4). The conductive fracture frequency, λ_C, is used to calculate a P32 representing the connected network. Even though λ_C may not be uniquely defined using the OXFILET approach, it can define the smallest frequency that represents the field data.

Air-permeability distribution data from boreholes USW NRG-6 and USW NRG-7/7a, (figs. 3 and 4), were converted to transmissivities and used to calculate λ for each borehole. The arithmetic-averaged value was used as simulation input. From the OXFILET approach, $\lambda_C = 0.29$ and the transmissivities of individual fractures were lognormally distributed and had a mean of 4.87×10^{-6} m^2/s and a standard deviation of 6.01×10^{-6} meters squared per second (m^2/s). A cutoff or minimum transmissivity of 4.00×10^{-6} m^2/s was used for borehole USW NRG-6 and 2.00×10^{-6} m^2/s for borehole USW NRG-7/7a (table 4). The connected fracture frequency then was used to calculate $P32_C$ in the connected network simulation (see table 5 for all simulation input parameters).

Fracture-Intensity Analysis

The connected fracture intensity, $P32_C$, is based on a ratio of initial fracture intensity and initial fracture frequency, λ_I. Where

$$P32_C = \lambda_C (P32_I / \lambda_I) \qquad (1)$$

The initial fracture frequency, λ_I, of the simulated network was derived from calculating fracture frequencies from a simulated horizontal borehole (onedimension) of some length. This calculation was repeated for several realizations and from different spatial orientations. The mean frequency that is calculated is used as the initial frequency.

A $P32_C$ was calculated for each fracture subunit based on statistical analysis of the DLS in the ESF and used as input into equation 1. The calculated $P32_C$ values for the subunits are listed in table 2. Subunit FSU 1 has a lower $P32_C$ than subunit FSU 2, even though the initial P32 values are reversed. In the calculations, the different fracture frequencies (λ_I) caused the intensities to reverse. The $P32_C$ value then was

Table 4. OXFILET simulation results for calculating the conductive fracture network

[--,no data; m^2/s, meters squared per second; std. dev., standard deviation]

Parameter	USW NRG 6		USW NRG 7/7a		Geometric mean
	Simulation	Field data	Simulation	Field data	
Number of data points	50	34	45	38	--
Minimum transmissivity (m^2/s)	$4.00x10^{-6}$	--	$2.00x10^{-6}$	--	--
Percent nonconductive	30	29	42.2	34.2	--
Transmissivity distribution type	Lognormal	Lognormal	Lognormal	Lognormal	--
Mean transmissivity (m^2/s)	$6.48x10^{-6}$	--	$3.66x10^{-6}$	--	$4.87x10^{-6}$
Std. dev (m^2/s)	$9.64x10^{-6}$	--	$3.75x10^{-6}$	--	$6.01x10^{-6}$
Number fractures per meter, P10	0.25	--	0.33	--	0.29
Smirnov, percent significance	94.7	--	96.7	--	--
Chi-squared, percent significance	68.3	--	82.9	--	--

Table 5. Fracture-set input parameters for network simulation, Topopah Spring Tuff, for all fracture subunits

[Dispersion, k = amount of clustering around a mean, smaller numbers represent tighter clustering; P32 = fracture area/rock volume. There are no specific fracture sets defined because fracture orientations were taken directly (bootstrapped) from the detailed line survey data for the Exploratory Studies Facility]

Orientation				Size						
Pole (trend plunge)	Azimuth (trend, plunge)	Dispersion k	Type	Minimum equivalent radius (meters)	Exponent (m)	Type	Minimum/maximum truncation (m)	Termination, percent	Strength, percent	Intensity P32, square meters per cubic meter
Bootstrap method	Bootstrap method	50	Bootstrap method	1.0	3.5	Power law	1.50 / 100.0	20	Bootstrap method	See table 2

used as input to simulate a connected network. Once a connected fracture network was finalized, the fracture network could be further analyzed, including the number and volume of connected networks and pathways, number and length of fracture intersections, size of blocks between fractures, and flow simulations (fig. 19).

Truncation of Small Fractures

The number of fractures generated in this connected network was large enough, using the estimated P32 intensities, to cause computational problems; therefore, the number of fractures in the system needed to be decreased, but the connectivity of the network needed to be kept intact. A numerical study was done to determine what effect minimum truncation size had on the connectivity of a fracture network. Realizations were generated with randomly oriented fractures and length parameters similar to the Topopah Spring Tuff (powerlaw distributed, with a minimum of 0.23 m and an exponent of 2.75). A maximum size truncation of 100 m was kept constant, while changing the minimum truncation to determine what effect there was, if any, on the number of pathways in the network. The first simulation had no truncation, but the lower truncation size in each simulation was increased by 0.25 m, up to 1.50 m. Therefore, in each new simulation, the smallest fractures were systematically removed. Fracture intensity (P32) was decreased so as not to bias the network. The intensity was decreased proportionally, corresponding to the decreased area under the length-distribution curve. For each simulation, a pathway analysis was done from one end of the generation region to the other. Results indicated that each simulation produced the same number of pathways, or connected networks, indicating that most small fractures did not contribute to the connectivity of the network. There was other corroborating evidence that this lack of contribution occurred. For example, in a small-scale two-dimensional network, Odling (1995, p. 40) stated that "even at high fracture densities, the flow properties of the fracture network are dominated by less than half the total fracture trace lengths." Therefore, truncating fractures as long as 1.50 m would have no effect on the connectivity or flow of the system. This truncation must come after an initial length distribution is determined from mapped lengths.

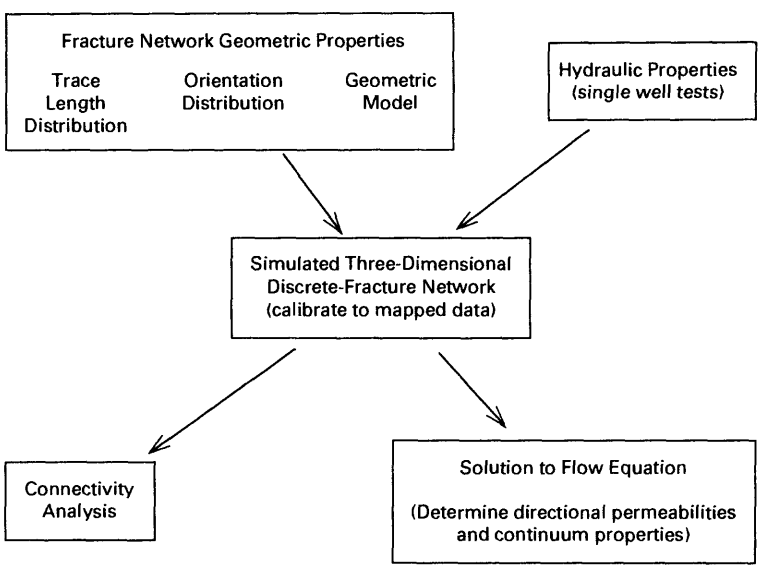

Figure 19. Flow chart showing how the discrete-fracture network is related

Geometric Evaluation

Connectivity

Connectivity (or conductivity) is related to fracture size, orientation, and intensity (Odling and Webman, 1990), although for any given, naturally occurring fracture network, fracture size is the most important variable (La Pointe and others, 1995). The geometry of the fracture system controls the flow of water in a rock volume for given boundary conditions and almost impermeable rock matrix. Because the ESF is essentially dry, no determination could be made between water-conductive and non-water-conductive fractures.Connectivity of a fracture network needs to be analyzed to help understand flow results. The analysis calculates the number of fracture networks that connect (a pathway) to each traceplane and the probability of connection (based on 20 realizations). The traceplane setup for blocks with edge lengths of 50, 100, 150, and 200 m (referred to as 50-, 100-, 150-, and 200-m scale) is shown in figure 20. The traceplanes include all six sides of a block plus three equally spaced horizontal planes. Each block has a common center point.

Results indicated that, in general, the number of connections between any two traceplanes, if there is a connection, is sparse (tables 6 and 7). The mean number of maximum connections ranged from 1 for all scales to 2.050 for the 50-m scale, to 5.737 for the 200-m scale. However, 80 percent of the realizations for the 200-m scale had no connection from the south to the north face. The number of connections and the pattern of connections indicated little appreciable change with scale. However, there were some differences. For example, there were more connections between adjacent traceplanes than opposite traceplanes, often by a factor of three or four. Also, the number of connections from the top to the middle-bottom for the 50-m-and 100-m-scale blocks was greater than connections from the 150-m-and 200-m-scale blocks. From the middle to the middle-top of the blocks, the number of connections increased with increase in scale. From the middle to the bottom, the number increased with increase in scale. For all scales, the number of connections increased as the distance between horizontal traceplanes decreased.

The mean probabilities that any two traceplanes of the various scales of the block are connected through a fracture network are listed in tables 8 and 9.

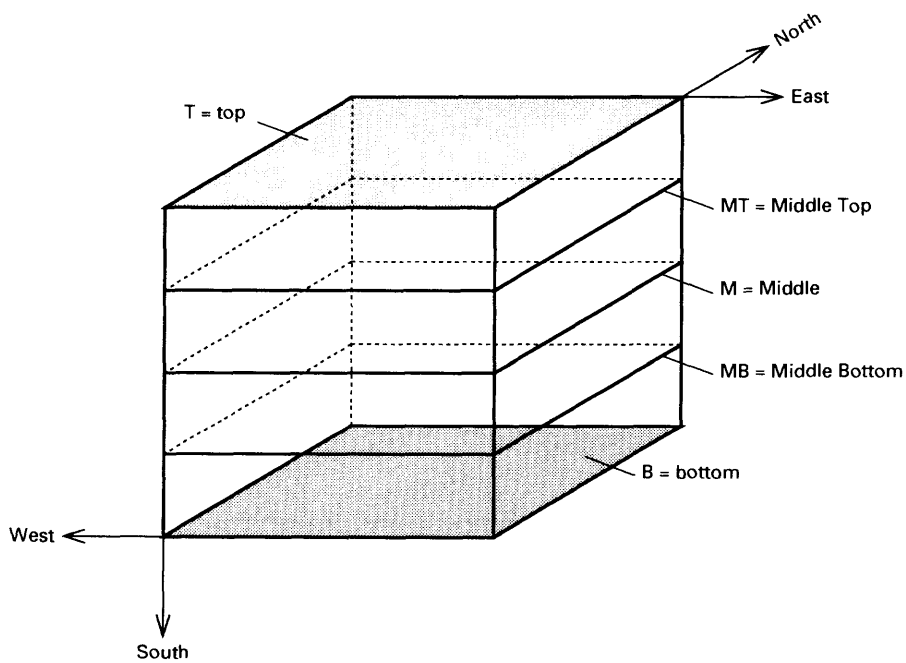

Figure 20. Nomenclature for traceplane faces in simulated region used in network and flow simulations at various scales. Each block had a common center point.

Table 6. Mean number of connections between any two traceplanes, if there is a connection (50-meter and 100-meter scale)

[If there is a connection between two traceplanes, then that connection receives a value equal to the number of independant pathways between the traceplanes. If there is no connection, the a null cell is entered. The mean is only calculated for those realizations that have connection. Refer to figure 20 for flow-block configuration]

50-meter scale									
Trace-plane	**East**	**South**	**North**	**West**	**Top**	**Bottom**	**Middle Bottom**	**Middle**	**Middle Top**
East		1.059	1.313	1.000	1.188	1.188	1.250	1.333	1.294
South	1.059		1.056	1.333	1.526	1.368	1.368	1.700	1.700
North	1.313	1.056		1.438	1.700	1.526	1.389	2.050	1.750
West	1.000	1.333	1.438		1.368	1.235	1.294	1.579	1.579
Top	1.188	1.526	1.700	1.368		1.059	1.063	1.316	1.850
Bottom	1.188	1.368	1.526	1.235	1.059		1.474	1.211	1.111
Middle Bottom	1.250	1.368	1.389	1.294	1.063	1.474		1.611	1.176
Middle	1.333	1.700	2.050	1.579	1.316	1.211	1.611		1.750
Middle Top	1.294	1.700	1.750	1.579	1.850	1.111	1.176	1.750	

100-meter scale									
Trace-plane	**East**	**South**	**North**	**West**	**Top**	**Bottom**	**Middle Bottom**	**Middle**	**Middle Top**
East		1.474	1.526	1.000	1.789	2.200	1.900	1.789	1.800
South	1.474		1.050	2.053	2.100	1.850	2.150	1.950	2.550
North	1.526	1.050		1.700	2.200	2.200	2.600	2.400	2.300
West	1.000	2.053	1.700		2.150	1.650	2.150	1.900	2.100
Top	1.789	2.100	2.200	2.150		1.050	1.100	1.600	2.200
Bottom	2.200	1.850	2.200	1.650	1.050		2.000	1.300	1.100
Middle Bottom	1.900	2.150	2.600	2.150	1.100	2.000		1.900	1.250
Middle	1.789	1.950	2.400	1.900	1.600	1.300	1.900		2.000
Middle Top	1.800	2.550	2.300	2.100	2.200	1.100	1.250	2.000	

Table 7. Mean number of connections between any two traceplanes, if there is a connection (150-meter and 200-meter scale)

[If there is a connection between two traceplanes, then that connection receives a value equal to the number of independant pathways between the traceplanes. If there is no connection, then a null cell is entered. The mean is only calculated for those realizations that have connection. Refer to figure 20 for flow-block configuration]

150-meter scale									
Trace-plane	**East**	**South**	**North**	**West**	**Top**	**Bottom**	**Middle Bottom**	**Middle**	**Middle Top**
East		2.100	2.400	1.000	2.250	2.800	2.450	3.100	2.450
South	2.100		1.211	2.316	4.400	3.400	3.650	3.450	3.900
North	2.400	1.211		2.300	3.850	3.947	3.600	3.800	3.550
West	1.000	2.316	2.300		3.300	2.550	2.700	2.600	3.150
Top	2.250	4.400	3.850	3.300		1.111	1.200	1.300	1.750
Bottom	2.800	3.400	3.947	2.550	1.111		1.789	1.421	1.158
Middle Bottom	1.450	3.650	3.600	2.700	1.200	1.789		2.350	1.500
Middle	3.100	3.450	3.800	2.600	1.300	1.421	2.350		2.400
Middle Top	2.450	3.900	3.550	3.150	1.750	1.158	1.500	2.400	
200-meter scale									
Trace-plane	**East**	**South**	**North**	**West**	**Top**	**Bottom**	**Middle Bottom**	**Middle**	**Middle Top**
East		3.211	2.778	1.000	2.222	4.000	3.121	3.263	3.316
South	3.211		1.118	3.056	3.368	5.474	4.947	5.737	4.421
North	2.778	1.118		2.684	4.105	5.053	4.421	5.000	4.474
West	1.000	3.056	2.684		2.833	3.444	3.158	3.474	3.474
Top	2.222	3.368	4.105	2.833		1.077	1.125	1.250	1.722
Bottom	4.000	5.474	5.053	3.444	1.077		1.789	1.412	1.135
Middle Bottom	3.421	4.947	4.421	3.158	1.125	1.789		2.526	1.789
Middle	3.263	5.737	5.000	3.474	1.250	1.412	2.526		3.000
Middle Top	3.316	4.421	4.474	3.474	1.722	1.235	1.789	3.000	

Table 8. Mean value of probability that any two traceplanes of the flow block are connected (50-meter and 100-meter scale) through a fracture network

[If there is a connection for a given realization, then that connection receives a value of one regardless of how many separate networks may connect the traceplanes. Refer to figure 20 for flow-block configuration. Based on 20 realizations]

50-meter scale

Trace-plane	East	South	North	West	Top	Bottom	Middle Bottom	Middle	Middle Top
East		0.85	0.8	0.5	0.8	0.8	0.8	0.9	0.85
South	0.85		0.9	0.9	0.95	0.95	0.95	1	1
North	0.8	0.9		0.8	1	0.95	0.9	1	1
West	0.5	0.9	0.8		0.95	0.85	0.85	0.95	0.95
Top	0.8	0.95	1	0.95		0.85	0.8	0.95	1
Bottom	0.8	0.95	0.95	0.85	0.85		0.95	0.95	0.9
Middle Bottom	0.8	0.95	0.9	0.85	0.8	0.95		0.9	0.85
Middle	0.9	1	1	0.95	0.95	0.95	0.9		1
Middle Top	0.85	1	1	0.95	1	0.9	0.85	1	

100-meter scale

Trace-plane	East	South	North	West	Top	Bottom	Middle Bottom	Middle	Middle Top
East		0.95	0.95	0.75	0.95	1	1	0.95	1
South	0.95		1	0.95	1	1	1	1	1
North	0.95	1		1	1	1	1	1	1
West	0.75	0.95	1		1	1	1	1	1
Top	0.95	1	1	1		1	1	1	1
Bottom	1	1	1	1	1		1	1	1
Middle Bottom	1	1	1	1	1	1		1	1
Middle	0.95	1	1	1	1	1	1		1
Middle Top	1	1	1	1	1	1	1	1	

Table 9. Mean value of probability that any two traceplanes of the flow block are connected through a fracture network. (150-meter and 200-meter scale

[If there is a connection for a given realization, then that connection receives a value of one regardless of how many separate networks may connect the traceplanes. Refer to figure 20 for flow block configuration. Based on 20 realizations]

150-meter scale									
Trace-plane	**East**	**South**	**North**	**West**	**Top**	**Bottom**	**Middle Bottom**	**Middle**	**Middle Top**
East		1	1	0.65	1	1	1	1	1
South	1		0.95	0.95	1	1	1	1	1
North	1	0.95		1	1	0.95	1	1	1
West	0.65	0.95	1		1	1	1	1	1
Top	1	1	1	1		0.9	1	1	1
Bottom	1	1	0.95	1	0.9		0.95	0.95	0.95
Middle Bottom	1	1	1	1	1	0.95		1	1
Middle	1	1	1	1	1	0.95	1		1
Middle Top	1	1	1	1	1	0.95	1	1	

200-meter scale									
Trace-plane	**East**	**South**	**North**	**West**	**Top**	**Bottom**	**Middle Bottom**	**Middle**	**Middle Top**
East		1	0.95	0.55	0.95	1	1	1	1
South	1		0.9	0.95	1	1	1	1	1
North	0.95	0.9		1	1	1	1	1	1
West	0.55	0.95	1		0.95	0.95	1	1	1
Top	0.95	1	1	0.95		0.7	0.85	0.85	0.95
Bottom	1	1	1	0.95	0.7		1	0.9	0.9
Middle Bottom	1	1	1	1	0.85	1		1	1
Middle	1	1	1	1	0.85	0.9	1		1
Middle Top	1	1	1	1	0.95	0.9	1	1	

If there is a connection for a given realization (from south to north, for example), then that connection is given a value of 1 regardless of how many separate networks may connect the traceplanes. Results indicate that the east-west direction had the lowest probability of connection, ranging from 50 percent for blocks at the 50-m scale to 75 percent for blocks at the 100-m scale. The top to bottom block direction had the next lowest mean probability at 85 percent for the 50-m scale and 70 percent for the 200-m scale. For all other directions and scales, the mean probabilities ranged from 80 to 100 percent.

Spatial Model

Because of the structural complexity at Yucca Mountain, spatial distribution of fractures can be an important aspect to understanding flux distribution and rates. The DLS mapping indicated the rate of variation of fracture spacing as ranging from sharp to gradual. Attempts were made to analyze the spatial distribution of the fracture data using: (1) Geostatistic analysis of borehole UE-25 UZ 16, and (2) fractal analysis of DLS of the ESF for the Topopah Spring Tuff.

A variogram analysis (fig. 21) of the air-permeability distribution in borehole UE-25 UZ 16 showed that there was no spatial correlation (no sill), although there were a small number of data points.

A fractal analysis of the DLS data indicated no correlation of ESF distance to fracture spacing using the box dimension method. However, the mass dimension method produced mixed results. When all segments of the ESF were combined, the mass dimension value was greater than 0.9, indicating that fracture spacing was random. The two different straight-line segments of the ESF then were analyzed. The northwest segment had a dimension of 0.85, whereas the north-south segment had a dimension of 0.95. A value of 0.85 would indicate a tendency toward fractal, but the spacing would still be considered random. Fractures were separated in classes by orientation (by visual segregation, as described above) and by the two different straight-line segments. Results indicated that sub-vertical fractures of the northwest segment had a slightly lower mean dimension of 0.84 and the north-south segment had a mean dimension of 0.92. Subhorizontal fractures from the northwest segment had a dimension of 0.75 and from the north-south segment a dimension of 0.92. The data indicated that the subhorizontal fractures were somewhat clustered in the northwest segment and were randomly distributed in the north-south segment. Because of these findings, no comprehensive spatial model could be determined

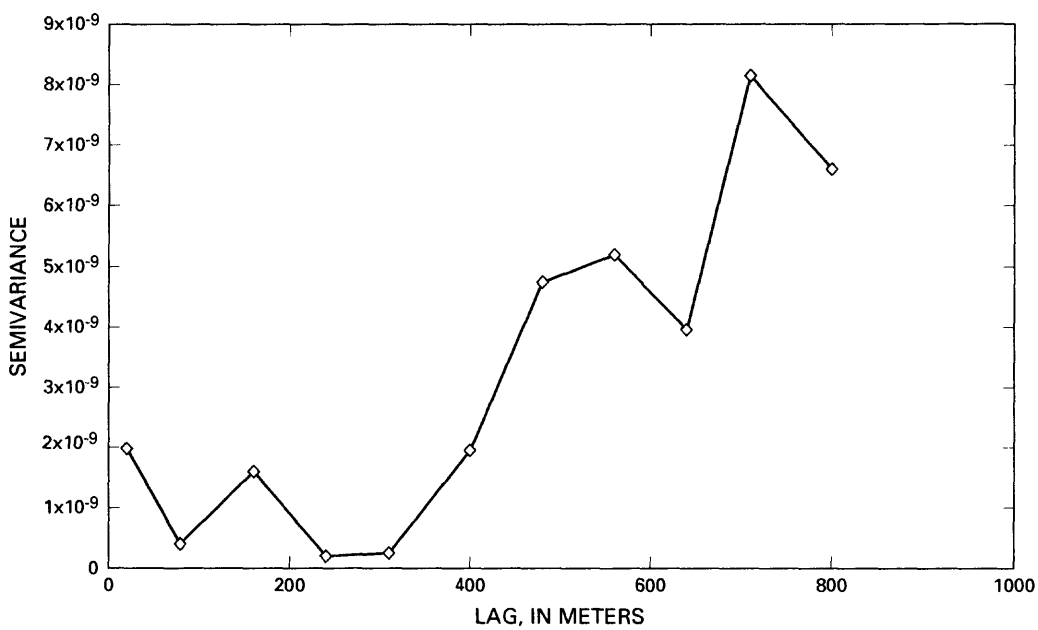

Figure 21. Semivariogram for air-permeability data from borehole UE-25 UZ#16.

in this preliminary study. As a result, the DFN models for this project used the stational Poisson process. That is, fractures were represented as planar and elliptically shaped polygons having centers that were randomly located in space, described by a stationary Poisson point process (Dershowitz and others, 1994). Fracture networks were generated stochastically as realizations of randomly located fracture sets.

Rock-Block Analysis

Rock-block analysis defined the size distribution of blocks bounded by fractures that divided the fracture network. The results (table 10) can be used to calculate an average rock-block size used in dual porosity simulations. The dimensions of the blocks were defined as the mean, standard deviation and minimum and maximum block sizes for length, area, and volume measurements. To calculate the block sizes, randomly oriented rays were placed in random positions, and one or two other rays were placed at orthogonal angles. The distance from the center point of each ray to a fracture was computed, and a length, area, and volume were calculated.

BLOCK-SCALE FLOW SIMULATION

Flow modeling of the Topopah Spring Tuff calculated flow properties of simulated blocks of different scales (50, 100, 150, and 200 m) to be used as input into equivalent-continuum models. Three methods were used to develop the flow properties: (1) Determine directional permeabilities for a unit gradient in the same direction for the different scales, (2) determine flux rates for different directions under a single unit gradient for the different scales, and (3) determine two-phase flow properties for different boundary conditions. Although the overall focus of this study was the unsaturated part of the Topopah Spring Tuff, only saturated flow conditions [using the MAFIC flow code (Miller, 1994)] were used by the first two methods.

Once the connected network was generated, a finite-element mesh was generated on the fractures to simulate flow numerically. A mesh generator called MESHMAKER (a module in FRACMAN) (Dershowitz and others, 1994) transforms fractures into meshes containing triangular finite elements. This transformation allowed the coupling of the flow code MAFIC (Miller and others, 1994) and the fracture network.

Directional Permeability

Directional permeability measures the anisotropy of the rock volume and can determine if one direction is more conductive than another. For each block scale, directional permeability was calculated using a unit gradient for each of three different directions, and from one end to the opposite end of the flow block.

Net directional permeability, K_g, was calculated in the direction of gradient using Darcy's law,

$$K_g = Q_g/(A \nabla J) \quad (2)$$

where Q_g is the water flux calculated from the finite-element analysis (based on assigned fracture permeability distributions), A is the gross area perpendicular to flow, and J is the gradient. The results of the permeability calculations can be used to determine scaling properties and evaluate anisotropy of the rock.

Table 10. Rock-block size analysis

[Block size represents distance, area, or volume between fractures, Topopah Spring Tuff; based on 20 realizations]

Parameters	Topopah Spring Tuff		
	One dimension (meters)	Two dimensions (square meters)	Three dimensions (cubic meters)
Mean	5.8	249.3	348.5
Standard deviation	3.6	341.1	855.8
Minimum	0.55	1.84	0.15
Maximum	21.1	2,291	6,704

For each position of the flow block a unit head gradient was assigned for a pair of opposite traceplanes with other traceplanes having no-flow boundaries. Similar procedures were used for directions of south to north, east to west, and top to bottom. Geometric mean permeability values were calculated from net permeability values for 10 realizations for each flow direction (fig. 22 and table 11). Results indicated that the east-west direction had a lower permeability than the north-south or top-bottom directions by a factor of five for all scales except the 200-m scale. The 200-m scale had the lowest permeability for all directions, especially the north-south direction. Except for the 200-m scale the east-west, north-south, and top-bottom permeabilities differed by about a factor of two. These data indicated that the range of values for each direction varied slightly with scale, except for the 200-m scale. The data also indicated that for each scale, some anisotropy existed, although the 200-m scale was anisotropic. The data also indicated that the east-west direction was the least conductive; whereas the north-south and the top-bottom directions were the most conductive, however, for the 200-m scale, the north-south direction was the least conductive and the top-bottom was the most conductive.

Mean permeability variations could be attributed to the mean probability of connection for a given scale. A tendency for mean permeability to increase as the mean probability of connection from one traceplane to another increases is shown in figure 23.

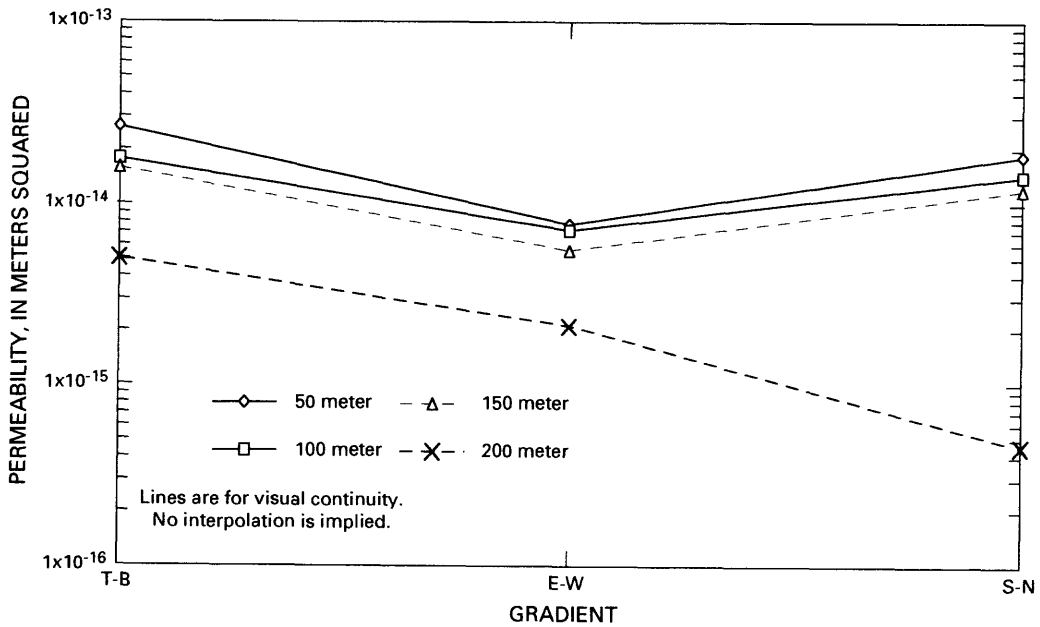

Figure 22. Mean permeability (from 10 realizations) calculated in the direction of gradient for four block sizes, T-B= top to bottom, E-W= east to west, S-N= south to north.

Table 11. Mean permeability values in direction of unit gradient for flow blocks that have varying scales

	Mean permeability (meters squared)			
Gradient from	**50-meter scale**	**100-meter scale**	**150-meter scale**	**200-meter scale**
Top to bottom	2.65×10^{-14}	1.77×10^{-14}	1.58×10^{-14}	5.01×10^{-15}
East to west	7.79×10^{-15}	7.20×10^{-15}	5.58×10^{-15}	2.11×10^{-15}
South to north	1.85×10^{-14}	1.43×10^{-14}	1.21×10^{-14}	4.57×10^{-16}

These results are conservative compared to dilution capabilities for a contaminant because the individual realizations had more variation in permeability for different directions than was apparent from mean values. Therefore, more anisotropy may exist than was apparent from these results.The order of magnitude difference between simulated directional permeability (table 11) and air-tested permeability (geometric mean for borehole USW NRG-6 was 9.5×10^{-13} m^2 and borehole USW NRG-7/7a was 3.43×10^{-13} m^2) is difficult to explain, although several possibilities or combinations of possibilities may exist. First, air-permeability tests were only meters in scale, whereas the simulated region was tens to hundreds of meters in scale. In addition, equating well tests with block-scale fractured rock has not yet been very successful. Second, because the fracture network in this system was sparse, there were a limited number of independent pathways consisting of only a few fractures, which means that the overall system functioned in a series and had a lower bulk permeability than the input data. Third, in-situ measurements calculated permeability for faults and fractures, whereas model permeability calculations were only for fractures. Fourth, effects of differential horizontal stress is an inherent part of in-situ testing, but, it was not included as part of this preliminary model.

Equivalent-Continuum Properties

An objective of this study was to determine, if possible, at what scale the Topopah Spring Tuff, as related to the fracture system, developed equivalent-continuum properties. The methods used for this determination were similar to the methods used to determine directional permeabilities. The differences in the methods were (1) different boundary conditions were used and (2) flux values were calculated for all directions for each gradient direction. In the directional-permeability analysis, all boundaries were no flow, except for the opposite traceplanes under a unit gradient. For this equivalant-continuum analysis, opposite traceplanes were still under unit gradient; however, all other traceplanes were specified as variable head. This specification allowed a flux value to be calculated in different directions other than the gradient direction. Other head gradients were imposed and fluxes calculated and compared.

A rock volume may be represented as an equivalent continuum if, for each gradient direction, flux

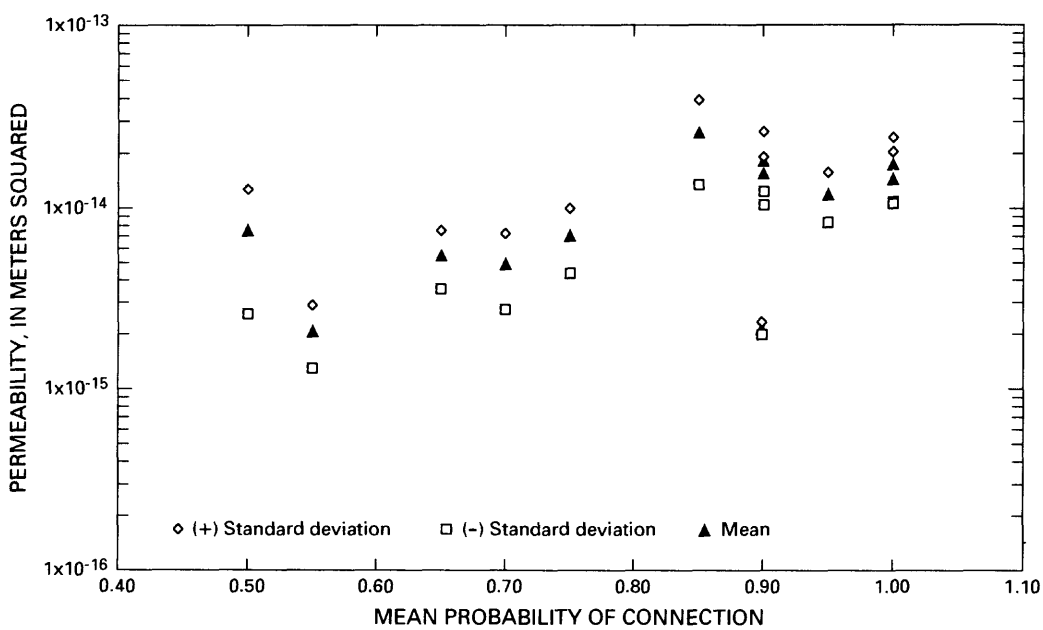

Figure 23. Mean directional permeability versus mean probability that any two traceplanes are connected through a fracture network, for all scales. Error bars are one standard deviation.

values are symmetric. That is, flux values in opposite directions are equal, and for a different gradient, flux values for different directions are equal (Bear, 1972). For example, if a unit gradient is imposed from the top to bottom of a block, then the flux values from the south direction must equal the flux from the north direction, and east values must equal west values. In addition, a unit gradient must be imposed in a different direction for example, (from south to north) and the flux values from the top and bottom must equal flux from the north and south directions calculated from the top to bottom gradient. Results comparing flux values are shown in figures 24 through 27 and in table 12. For each gradient direction, flux values in opposite directions for the 50-m scale did not vary by more than a factor of four; for the 100-m scale, not more than a factor of two; for the 150-m scale, not more than one order of magnitude, and for the 200-m scale, not more than two orders of magnitude.

Directional flux values, when compared with different gradient directions for the 50-m scale, varied as much as a factor of six; for the 100-m scale as much as a factor of three; for the 150-m scale as much as a factor of five; and for the 200-m scale, by three orders of magnitude.

The data also indicated that directional fluxes from the 100-m scale varied the least, where as the 200-m scale varied the most. There was a gradual increase in geometric mean flux from the 50-m scale to the 150-m scale. The 200-m scale had very erratic values. For all scales, when the gradient was from top to bottom, north and south flux was greater than east and west flux. However, the 100-m scale had the least variation, whereas the 200-m scale had the greatest. The variations at the 200-m scale were probably due to several realizations that had no-flow results, especially from the north and south traceplanes.

As in the directional-permeability analysis, reporting mean flux values tended to smear anomalies for each realization. Therefore, the results from this study are conservative as to dilution capabilities for a contaminant. However, none of the scales tested (50, 100, 150, and 200 m) approached equivalent continuum properties and, only in a few analyses were the criteria met for an equivalant pourous medium where flux values from opposite directions varied by less than a factor of two. Based on these results, the tuffs probably would never approach equivalent continuum properties because of the heterogeneity of the simulated fracture system.

Water Flux in Unsaturated Conditions

Two-phase flow analysis is extremely difficult to conduct in complex fracture networks. Because there were no two-phase flow codes that solved the flow equations in complex discrete fracture networks, the flow of water was simulated in partly saturated conditions. In this method, however, the flow of air was not considered. The method calculated a new transmissivity (as described below) and flow equations were solved using the MAFIC flow code (Miller and others, 1994). The simulation domain was the same three-dimensional flow block as described in the "Directional Permeability" section. Only the 200-m scale was used. All simulations were run under a unit gradient from top to bottom, while controlling certain variables such as: (1) Making side boundaries no flow, (2) varying head at side boundaries, (3) varying the saturation field with depth. The relatively high saturations were modified from calculations from J.P. Rousseau (written commun., 1996) (boreholes USW NRG 6 and USW NRG-7/7a, fig. 28) and (4) holding saturation field constant at 0.20, which represented a relatively low saturation field.

Partly saturated conditions were replicated during the meshing process. The procedure was first to assign a value of saturation to every element based on values in the three-dimensional saturation field. The assigned saturation was based on the field saturation closest to the centroid of the element. Next, a relative permeability was specified for each element based on a linear interpolation of figure 29. Finally, a value of transmissivity (T) was specified for each element based on the equation $T = T_0 (K_{rel})$, where T_0 is original T, and K_{rel} is relative permeability of water.

To simplify the procedure, several assumptions were made. (1) The saturation fields that were used probably represented two extremes. The maximum saturation field was developed from in-situ measurements from boreholes USW NRG-6 and USW NRG 7/7a, then modified into a three-dimensional saturation field that had 10-m horizontal spacing and vertical spacing dictated by the in-situ measurements in figure 28. The minimum saturation field was 0.20, based on scoping calculations by Bodvarsson and Bandurraga (1996) and was held constant. (2) The

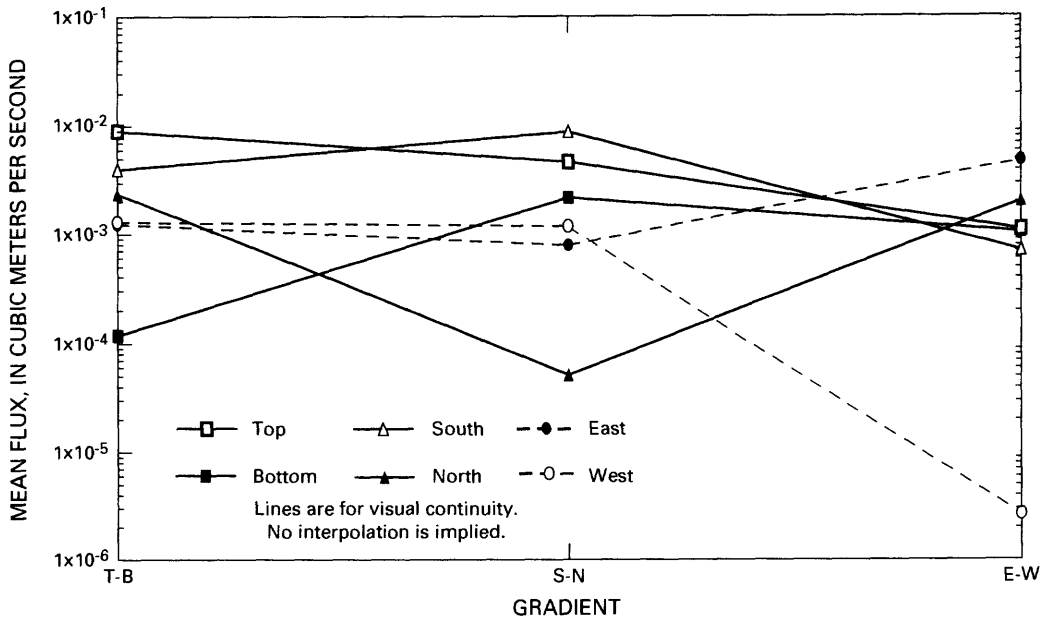

Figure 24. Mean directional flux values under unit gradient out of six flow-block traceplanes, for three gradient directions, Topopah Spring Tuff, 50-meter scale. T-B=top to bottom, S-N=south to north, E-W=east to west.

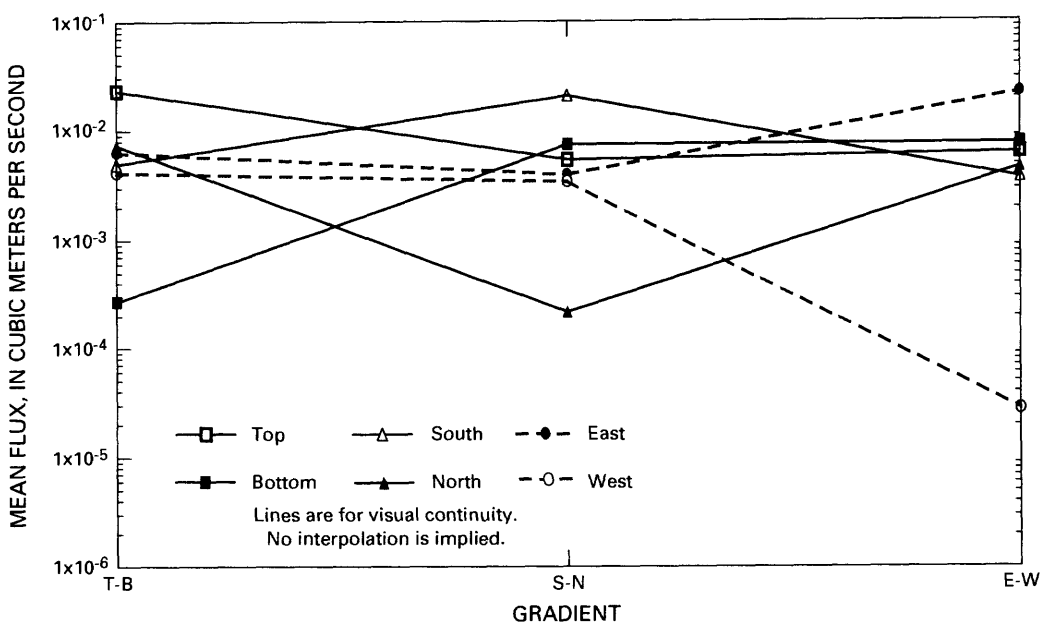

Figure 25. Mean directional flux values under unit gradient out ouf six flow-block traceplanes, for three gradient directions, Topopah Spring Tuff, 100-meter scale. T-B=top to bottom, S-N=south to north, E-W= east to west.

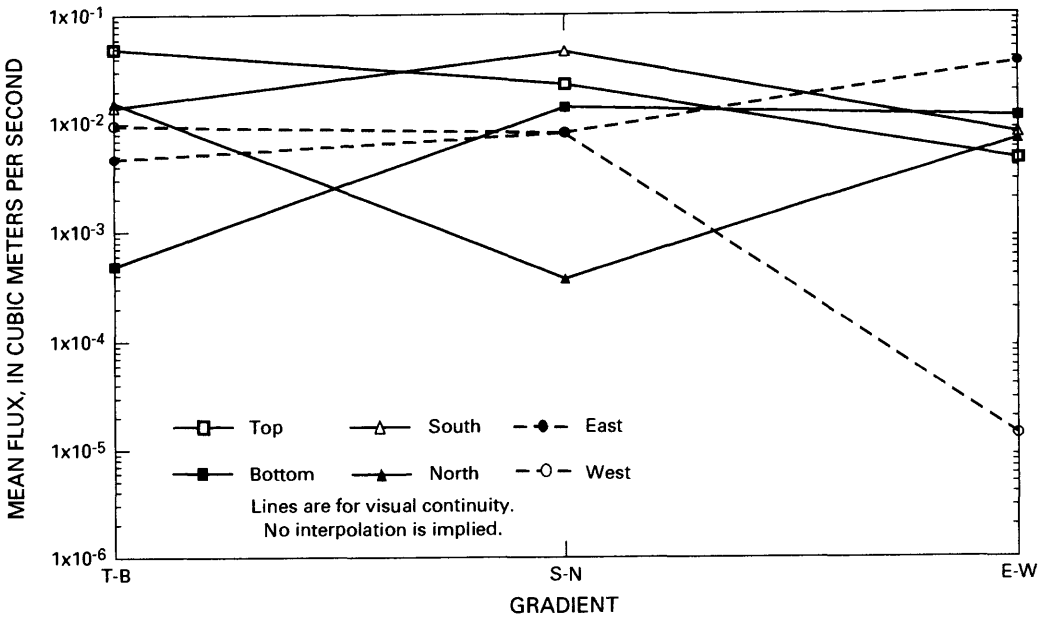

Figure 26. Mean directional flux values under unit gradient out of six flow-block traceplanes, for three gradient directions, Topopah Spring Tuff, 150-meter scale. T-B=top to bottom, S-N=south to north, E-W=east to west.

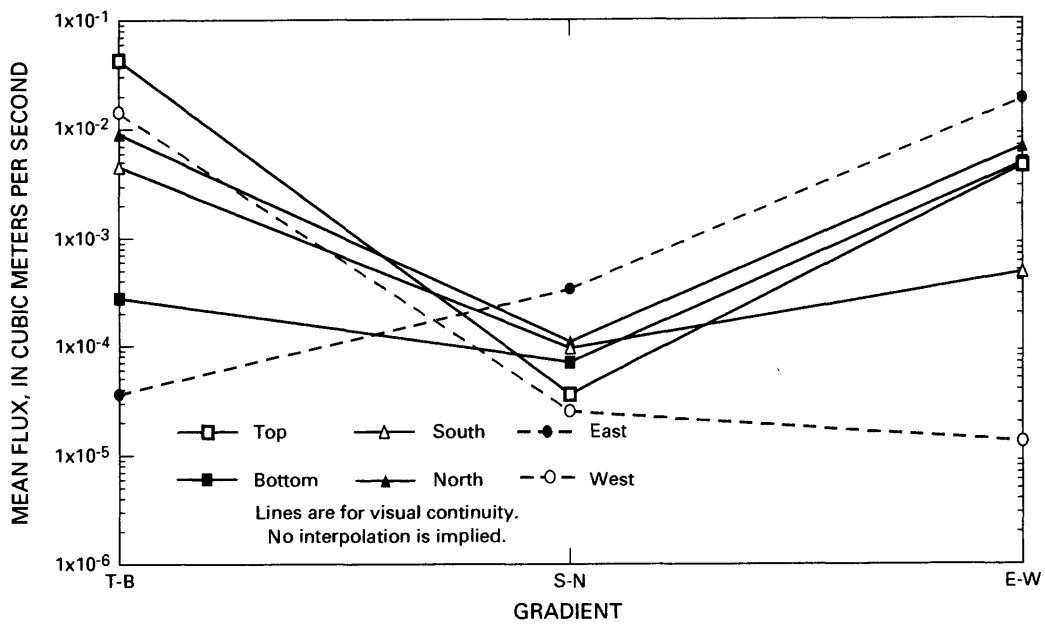

Figure 27. Mean directional flux values under unit gradient out of six flow-block traceplanes, for three gradient directions, Topopah Spring Tuff, 200-meter scale. T-B=top to bottom, S-N=south to north, E-W=east to west.

Table 12. Mean directional flux values (m^3/s) calculated under unit gradients imposed from top to bottom (T-B), south to north (S-N), and east to west (E-W), for flow blocks with 50-, 100-, 150-, and 200-meter scale

	Mean permeability (meters squared)					
Gradient from	**Top**	**Bottom**	**South**	**North**	**East**	**West**
			50-meter scale			
T-B	8.99E-03	1.18E-04	3.99E-03	2.37E-03	1.23E-03	1.29E.03
S-N	4.71E-03	2.19E-03	8.88E-03	5.17E-05	7.90E-04	1.18E-03
E-W	1.11E-03	1.05E-03	7.09E-04	2.03E-03	4.83E-03	2.66E-06
			100-meter scale			
T-B	2.31E-02	2.72E-04	4.96E-03	7.43E-03	6.35E-03	4.17E-03
S-N	5.46E-03	7.56E-03	2.07E-02	2.19E-04	4.00E-03	3.46E-03
E-W	6.36E-03	7.72E-03	3.76E-03	4.69E-03	2.19E-02	2.75E-05
			150-meter scale			
T-B	4.94E-02	4.90E-04	1.43E-02	1.58E-02	4.70E-03	9.66E-03
S-N	2.31E-02	1.43E-02	4.65E-02	3.73E-04	8.22E-03	8.22E-03
E-w	4.70E-03	1.16E-02	8.21E-03	7.14E-03	3.65E-02	1.39E-05
			200-meter scale			
T-B	4.26E-02	2.78E-04	4.59E-03	9.08E-03	3.61E-05	1.43E-02
S-N	3.61E-05	7.05E.05	9.56E-05	1.10E-04	3.37E-04	2.52E-05
E-W	4.59E-03	4.84E-03	4.78E-04	6.83E-03	1.86E-02	1.32E-05

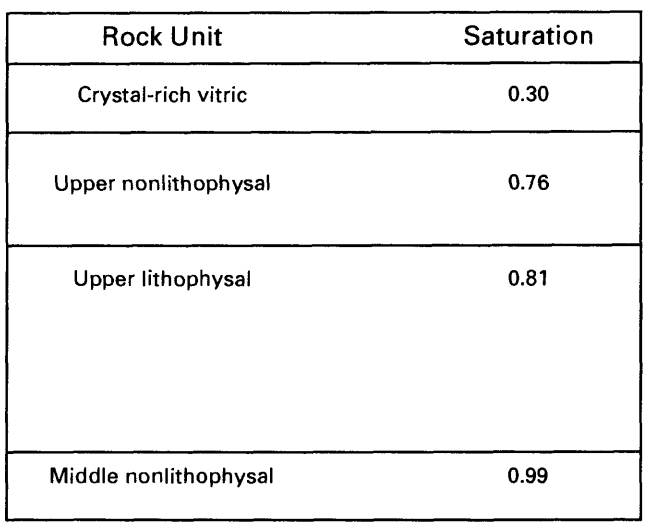

Figure 28. Saturations used in two-phase flow simulations through fractured Topopah Spring Tuff. Modified from J.P. Rosseau, U.S. Geological Survey, written commun., 1996. Space between units indicates relative thickness.

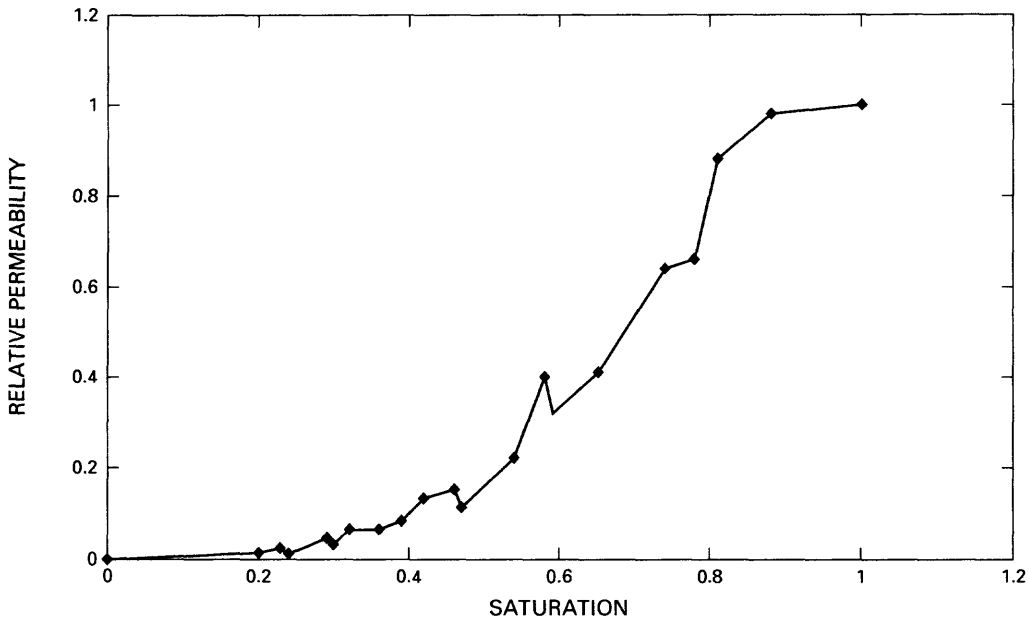

Figure 29. Relative permeability to water versus saturation for fractures in the Topopah Spring Tuff. Modified from E.W. Kwicklis (U.S. Geological Survey, written commun., 1996).

relative permeability to saturation data set (fig. 29) was the best available, although it is unknown if the curve is representative of in-situ conditions.

Results from this procedure were presented as mean values for the four different cases. For the no-flow side boundaries, the mean flux (into the top and out the bottom) was 9.37×10^{-4} cubic meters per second (m^3/s) using high saturation values, and 1.61×10^{-5} m^3/s for low saturation values. For variable head boundaries on the sides, the mean flux ranged from 3.32×10^{-5} m^3/s (south traceplane) to 1.05×10^{-3} m^3/s (north traceplane) for high saturations, and ranged from 2.62×10^{-6} m^3/s (bottom traceplane) to 2.40×10^{-4} m^3/s (top traceplane) for low saturations (fig. 30). These values represented mean bulk flux rates for 40,000 m^2 of rock area in the DFN.

For different saturations with variable head boundaries on the sides, flux values from the low saturation field were about one to one and one-half orders of magnitude lower from all traceplane directions than values from the high saturation field. For different saturations with no-flow boundaries on the sides, flux values varied by almost two orders of magnitude. Therefore, about one-half of the flux was leaving the 200-m scale block out the sides compared to the bottom (when specified head conditions were used at the side boundaries). The loss of flux out the side is not surprising because connectivity analysis indicated that there were just as many fracture connections in the horizontal direction as there were in the vertical direction. Also, there were more connections from the top to adjacent sides than from the top to the bottom of the block. Therefore, at the 200-m-block scale, there were equal opportunities for water to migrate down as well as laterally under natural conditions.

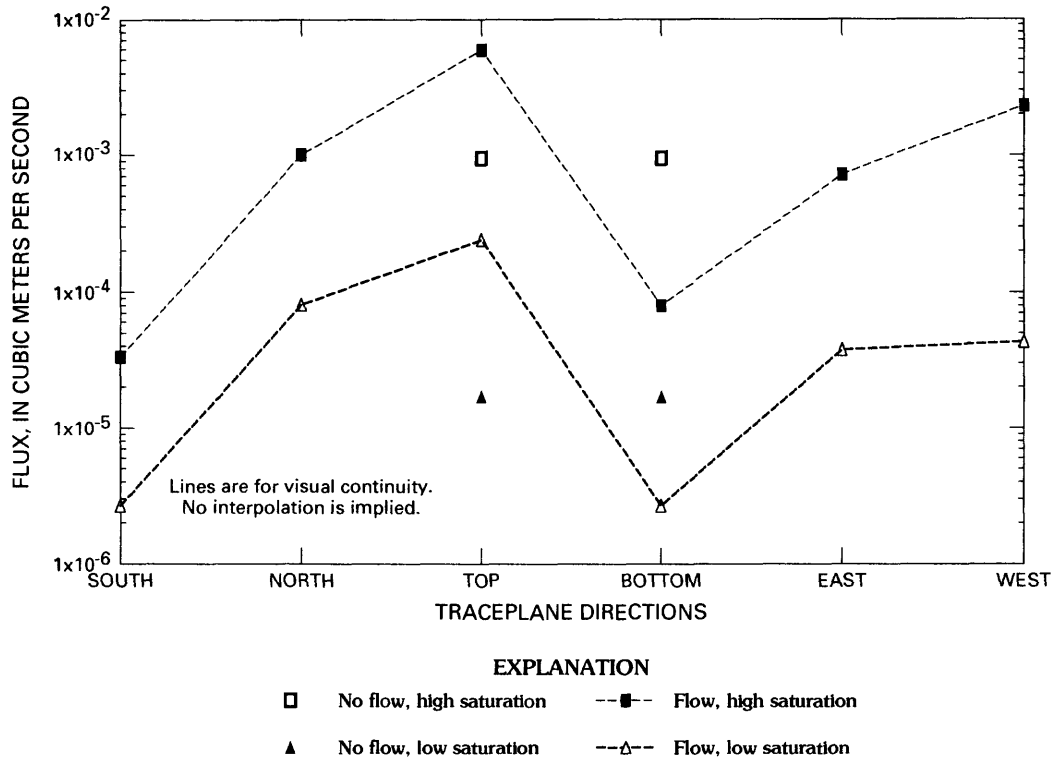

Figure 30. Mean water flux values from various traceplane directions under a unit gradient from top to bottom, 200-meter scale. No flow means no-flow boundaries and flow means variable head boundaries at north, south, east, and west traceplanes.

SUMMARY

This report is part of a preliminary modeling effort to investigate the effects of fractures on flow of water and air at Yucca Mountain, Nevada. A three-dimensional fracture network of the Topopah Spring Tuff in the vicinity of the ESF was simulated. The simulated network reasonably replicated the real fracture network because simulated fracture intensities matched well with mapped fracture intensities. A three-dimensional connected fracture network was simulated by eliminating nonconductive fractures determined from field-derived air permeabilities. The connected fracture network had numerous networks (fractures connected to each other), but few pathways that connected from opposite and adjacent traceplanes within flow blocks. For all block scales analyzed (50, 100, 150, and 200 m) an average of one continuous pathway connected one end to the opposite end. The number of pathways increased fourfold for adjacent traceplanes. Results indicated that, in general, the number of connections between any two traceplanes, if there was a connection, was sparse. The data also indicated that for each scale, some permeability anisotropy existed; the east-west direction was the smallest, and the top-bottom and north-south directions were the largest. The exception was the 200-m scale, which had the largest difference in permeability; the north-south direction had the smallest difference.

Small fractures could be eliminated from the simulated network without any effect on the overall connectivity. Fractures as much as 1.50 m long were eliminated from the fracture network without altering the number of connected networks, but substantially decreasing the number of fractures in the network. This result confirmed the theory that fracture length was one of the more important factors in determining network connectivity, which, in turn, controlled flow paths and rates. Block permeability simulations of saturated flow indicated that the network had a small range (less than a factor of two) in mean permeability for three principal directions.

The data indicated that the east-west direction was the least conductive, whereas the top-bottom and the north-south directions were the most conductive. For the 200-m block scale the north-south direction was the least conductive and the top-bottom was the most conductive.

None of the block scales tested (50, 100, 150, and 200 m) approached equivalen-continuum properties and, only in a few cases, were the criteria met where flux values from opposite directions varied by less than a factor of two. Based on these results, tuffs at Yucca Mountain probably would never approach equivalent-continuum properties because of the heterogeneity of the simulated fracture system.

Results of the two-phase flow simulations indicated that, for different saturations with variable head boundaries, flux values from the low saturation field were about two to one and one-half orders of magnitude lower from all traceplane directions than values from the high saturation field. For different saturations with no flow boundaries on the sides, flux values varied by two orders of magnitude when comparing transmissivities calculated from low saturations to transmissivities calculated from high saturations. Therefore, about one-half of the flux was leaving the 200-m-scale block out of the sides compared to the bottom (when specified head conditions were used at the side boundaries).

REFERENCES CITED

Anna, L.O., 1997, Preliminary three-dimensional discrete fracture model, Tiva Canyon Tuff, Yucca Mountain area, Nye County, Nevada: U.S. Geological Survey Open-File Report, in progress.

Anna, L.O., and Wallmann, Peter, 1997, Characterizing the fracture network at Yucca Mountain, Nevada, part 2 Numerical simulation of flow in a three-dimensional discrete fracture network, *in* Hoak, T.E., and Blomquist, P.K., eds, Fractured reservoirs— Descriptions, predictions, and applications: Denver, Colorado, Rocky Mountain Association of Geologists 1996 Guidebook, p. 199–207.

Barton, C.C., Larsen, E., Page, W.R., and Howard, T.M., 1993, Characterizing fractured rock for fluid flow, geomechanical, and paleostress modeling—Methods and preliminary results from Yucca Mountain, Nevada: U.S. Geological Survey Open-File Report 93–269, 62 p.

Bear, J., 1972, Dynamics of fluids in porous media: New York, New York, Dover Publications, Inc. 764 p.

Bodvarsson, G.S., and Bandurraga, T.M., eds., 1996, Development and calibration of the three-dimensional site-scale unsaturated zone model of Yucca Mountain, Nevada: Berkeley, Calif., Lawrence Berkeley National Laboratory LBNL Report–39315, 547 p.

Buesch, D.C., Spengler, R.W., Moyer, T.C., and Geslin, J.K., 1996, Revised stratigraphic nomenclature and macroscopic identification of lithostratigraphic units of the Paintbrush Group exposed at Yucca Mountain, Nevada: U.S. Geological Survey Open File Report 94–469, 45 p.

Carr, W.J., 1984, Regional structural setting of Yucca Mountain southwestern Nevada, and Late Cenozoic rates of tectonic activity in part of the southwestern Great Basin, Nevada and California: U.S. Geological Survey Open-File Report 84–854, 109 p.

Dershowitz, W., Lee, G., Geier, J., Hitchcock, S., and La Pointe, P.R., 1994, FRACMAN version 2.4— Interactive discrete feature data analysis, geometric modeling and exploration simulation: Redmond, Wash., Golder Associates, Inc., User Documentation, 171 p.

Efron, B., 1982, The jackknife, the bootstrap, and other resampling plans: Rapid City, S. Dak., Society of Industrial and Applied Mathematics Monograph no. 38, 26 p.

Fisher, R.A., 1953, Dispersion on a sphere: London, Proceedings of the Royal Society of London, Series A, v. 217, p. 29–306.

Frizzell, V.A. Jr., and Shulters, Jacqueline, 1990, Geologic map of the Nevada Test Site, southern Nevada: U.S. Geological Survey Miscellaneous Investigations Series Map I–2046, scale 1:100,000.

King, P.B., 1975, Ancient southern margin of North America: Geology, v. 3, no. 12, p. 732–734.

La Pointe, P.R., and Hudson, J.A., 1985, Characterization and interpretation of rock mass joint patterns: Boulder, Colorado, Geological Society of America Special Paper 199, 37 p.

La Pointe, P.R., Wallmann, Peter, and Follin, S., 1995, Estimation of effective block conductivities based on discrete network analyses using data from the Aspo site: Stockholm, Sweden, SKB [Svensk karnbranslehantesing AB] Stripa Technical Report 95–15, 141 p.

LeCain, G.D., 1995, Pneumatic testing in 45-degree inclined boreholes in ash flow tuff near Superior, Arizona: U.S. Geological Survey Water-Resources Investigations Report 95–4073, 27 p.

Miller, I., Lee, G., Dershowitz, W., and Sharp, G., 1994, Matrix/fracture interaction code (MAFIC) with solute

transport version β1.4: Redmond, Wash., Golder Associates, Inc., User Documentation, version 58 p.

Montazer, Parviz, and Wilson, W.E., 1984, Conceptual hydrologic model of flow in the unsaturated zone, Yucca Mountain, Nevada: U.S. Geological Survey Wate-Resources Investigations Report 84–4345, 55 p.

Nelson, P.H., and Anderson, L.A., 1992, Physical properties of ash flow tuffs from Yucca Mountain, Nevada: Journal of Geophysical Research, v. 97, no. B5, p. 6823–6841.

Odling, N.E., 1995, The development of network properties in natural fracture patterns, *in* Myer, L.R., Tsang, C.F., Cook, N.G., and Goodman, R.E., eds., Fractured and jointed rock masses, Proceedings of the conference on fractured and jointed rock masses, Lake Tahoe, Calif., June 3, 1992: Brookfield, A.A. Balkema, p. 35–41.

Odling, N.E., and Webman, I., 1990, A conductance mesh approach to the permeability of natural and simulated fracture patterns: Water Resources Research, v. 27, p. 2633–2643.

O'Neill, J.M., Whitney, J.W., and Hudson, M.R., 1992, Photogeologic and kinematic analysis of lineaments at Yucca Mountain, Nevada— Implications for strike-slip faulting and oroclinal bending: U.S. Geological Survey Open-File Report 91–623, 24 p.

Ortiz, T.S., Williams, R.L., Nimick, F.B., Whittet, B.C., and South, D.L., 1985, A three-dimensional model of reference thermal/mechanical and hydrological stratigraphy at Yucca Mountain, southern Nevada: Albuquerque, N. Mex., Sandia National Laboratories SAND84–1076, 76 p.

Osnes, J.D., Winberg, A., and Anderson, J., 1988, Analysis of well test data - application of probabilistic models to infer hydraulic properties of fractures: Rapid City, S. Dak., RE/SPEC, Inc., Topical Report RSI–0338, 56 p.

Rautman, C.A., and Flint, A.L., 1992, Deterministic geologic processes and stochastic modeling: Albuquerque, N.M., Sandia National Laboratories SAND91–1925C

Riehle, J.R., 1973, Calculated compaction profiles of rhyolitic ash flow tuffs: Boulder, Colo., Geological Society of America Bulletin, v. 84, no.3, p. 219–2216.

Riehle, J.R., Miller, T.F., and Bailey, R.A., 1995, Cooling, degassing, and compaction of rhyolitic ash flow tuffs— A computational model: Volcanology Bulletin, v. 57, no.2, p. 319–336.

Scott, R.B., 1990, Tectonic setting of Yucca Mountain, southwest Nevada, *in* Wernicke, B.P., ed., Basin and range extensional tectonics near the latitude of Las Vegas, Nevada: Boulder, Colo., Geological Society of America Memoir 176, p. 251–282.

Scott, R.B., and Bonk, Jerry, 1984, Preliminary geologic map of Yucca Mountain, Nye County, Nevada with geologic sections: U.S. Geological Survey Open-File Report 84–494, 10 p.

Snyder, D.B., and Carr, W.J., 1984, Interpretation of gravity data in a complex volcanic-tectonic setting, southwestern Nevada: Journal of Geophysical Research, v. 89, no. B12, p. 10193–10206.

Spengler, R.W., and Fox, K.F., 1989, Stratigraphic and structural framework of Yucca Mountain, Nevada: Radioactive Waste Management and the Nuclear Fuel Cycle, v. 13, nos. 1–4, p. 21–36.

Terzaghi, R.D., 1965, Sources of error in joint surveys: Geotechnique, v. 15, p. 287–303.

Throckmorton, C.K., and Verbeek, E.R., 1995, Joint networks in the Topopah Spring Tuffs of the Paintbrush Group, southwestern Nevada: U.S. Geological Survey Open-File Report 95–2, 179 p.

Wittwer, C.S., Chen, G., and Bodvarsson, G.S., 1993, Studies of the role of fault zones on fluid flow using the site-scale numerical model of Yucca Mountain: *in* American Nuclear Society annual international conference, High Level Radioactive Waste Management, 4th, La Grange Park, Ill., 1993, Proceedings: Las Vegas, Nev., American Nuclear Society, p. 667–674.

Wright, L.A., 1976, Late Cenozoic fault patterns and stress field in the Great Basin and westward displacement of the Sierra Nevada block: Geology, v. 4, no. 3, p. 489–494.

☆ U.S. GOVERNMENT PRINTING OFFICE: 1998 - 673-083 / 20015 REGION NO. 8